

University of Nevada, Reno

**Geometrically Accurate and Homogenized Fuel Region Models
to Predict Fuel Cladding Temperatures within a Truck cask
under Normal and Fire Accident Conditions**

A thesis submitted in partial fulfillment of the
requirements for the degree of Master of Science in
Mechanical Engineering

by

Krishna Kumar Kamichetty

Dr. Miles Greiner/Thesis Advisor

May 2010



University of Nevada, Reno
Statewide • Worldwide

THE GRADUATE SCHOOL

We recommend that the thesis
prepared under our supervision by

KRISHNA KUMAR KAMICHETTY

entitled

**Geometrically-Accurate And Homogenized Fuel Region Models To Predict
Cladding Temperatures Within A Truck Cask Under Normal And Fire Accident
Conditions**

be accepted in partial fulfillment of the
requirements for the degree of

MASTER OF SCIENCE

Dr. Miles Greiner, Advisor

Dr. Richard A Wirtz, Committee Member

Dr. George Danko, Graduate School Representative

Marsha H. Read, Ph. D., Associate Dean, Graduate School

May, 2010

Dedicated to my Parents

ABSTRACT

The temperature of spent nuclear fuel cladding within transport casks must be determined for both normal conditions of transport and hypothetical fire accident conditions to assure that it does not exceed certain limit conditions. In the current work a two-dimensional finite-element thermal model of a legal-weight truck cask is constructed that accurately models the geometry of the fuel rods and cover gas. Computational fluid dynamics (CFD) simulations are performed that include buoyancy induced motion in, and radiation and natural convection heat transfer across the cover gas, as well as conduction in all solid components. Separate simulations are performed using helium or nitrogen cover gas. Stagnant-gas CFD (SCFD) simulations are performed and compared to CFD simulations to determine the effect of gas motion. These results are compared to those from finite element models that employ Effective Thermal Conductivity properties in the fuel regions.

For normal conditions of transport, the peak clad temperature is determined for a range of fuel heat generation rates to determine the thermal dissipation capacity based on peak cladding and surface temperature, Q_C and Q_S . These are respectively, the fuel heat generation rates that bring the peak cladding temperature to 400°C, or the peak surface temperature to 85°C (their allowed limits for normal transport). Transient fire/post fire simulations are then performed for a range of fire durations to determine the critical durations for cladding Creep Deformation or Burst Rupture, D_{CD} or D_{BR} . These are the fire durations that bring the cladding temperature to 570°C or 750°C, respectively.

In the current work, a geometrically-accurate two-dimensional model is developed of a single fuel assembly within isothermal compartment walls. Finite element

thermal simulations are performed to determine the cladding temperature for a range of compartment wall temperatures and assembly heat generation rates. These results are used to determine a temperature-dependent effective thermal conductivity of the fuel region. The effective volumetric specific heat of the region is determined from a lumped capacity model. These effective properties are then applied to a two-dimensional model of a legal weight truck cask with homogenized (smeared) fuel regions. Steady state normal conditions of transport simulations are performed for a range of fuel heat generation rates. The generation rate that brings the Zircaloy cladding tubes to their radial hydride formation temperature is determined. Transient regulator fire accident simulations are performed for a range of fire durations. The minimum fire durations that bring the fuel cladding to its creep deformation or burst rupture temperatures are determined.

ACKNOWLEDGEMENT

Words are only representations of our regards and gratitude that we have towards our actions and their inherent associations. As a matter of fact, without co-operation, no thought could be coined into real action. Consistent motivation and invaluable support throughout any project is an issue that cannot quantitatively measured. These acknowledgements are only a fraction of regards towards their gestures.

I convey my sincere gratitude and thanks to *Dr. Miles Greiner* for having me as a part of his team and for providing me with all the support professionally and personally. It was this constant support and guidance that helped me and showed me the path to finish my master's degree.

I thank Professor *Richard A. Wirtz* and Professor *George Danko* for accepting to be part of my Master's thesis committee.

I would also like to acknowledge Narayana Rao Chalasani and Venkata Venigalla for their help through these years professionally and personally.

Finally, I am grateful to the Department of Mechanical Engineering, University of Nevada Reno for funding my work with support from US Global Nuclear Energy Partnership (GNEP) under contract DE-FC07-06ID14782.

Krishna Kumar Kamichetty

TABLE OF CONTENTS

1. INTRODUCTION	
1.1. Motivation	1
1.2. Background	2
1.3. Objective	5
2. COMPUTATIONAL MODELS	
2.1 Legal Weight Truck Package	8
2.2 Geometrically-Accurate Isolated Fuel compartment model	9
2.3 Effective Thermal Conductivity Isolated compartment model	10
2.4 Effective Thermal Conductivity Truck Package	10
3. COMPUTATIONAL METHODS	
3.1 Legal Weight Truck Package	11
3.2 Geometrically-Accurate Isolated Fuel compartment model	12
3.3 Effective Thermal Conductivity Isolated compartment model	14
3.4 Effective Thermal Conductivity Truck Package	15
3.5 Cask Boundary Conditions	
3.5.1 Normal Conditions of Transport	16
3.5.2 Shaded Conditions	17
3.5.3 Hypothetical Fire Accident Conditions	17
4. SIMULATION RESULTS	
4.1 Legal Weight Truck Package	
4.1.1 Normal Conditions of Transport	18

4.1.2 Hypothetical Fire Accident Conditions	
4.1.2.1 Regulatory Fire Duration	21
4.1.2.2 Long Duration Fires	22
4.2 Geometrically-Accurate Isolated Fuel Compartment Model	23
4.3 Effective Thermal Conductivity Isolated Compartment Model	24
4.4 Effective Thermal Conductivity Truck Package	
4.4.1 Normal Conditions of Transport	26
4.4.2 Hypothetical Fire Accident Conditions	
4.4.2.1 Regulatory Fire Duration, $D = 0.5$ hr	28
4.4.2.2 Long Duration Fires, 0.5 hr $< D < 20$ hr	29
5. SUMMARY AND CONCLUSIONS	31
6. FUTURE WORK	34
7. REFERENCES	35
TABLES	39
FIGURES	44

LIST OF TABLES

Table 1	Heat generation rate and durations of concern at initial peak cladding temperature, $T_{PC,I} = 400^{\circ}\text{C}$ for Accurate Geometry	39
Table 2	Heat generation rate and durations of concern at initial peak surface temperature, $T_{PS,I} = 85^{\circ}\text{C}$ for Accurate Geometry	40
Table 3	Material properties used in the geometrically accurate and homogenized isolated fuel compartment models	41
Table 4	Heat generation rate and duration of concern at initial peak cladding temperature, $T_{PC,I} = 400^{\circ}\text{C}$ for AG and HG models	42
Table 5	Heat generation rate and duration of concern at initial peak surface temperature, $T_{PS,I} = 85^{\circ}\text{C}$ for AG and HG models	43

LIST OF FIGURES

Figure 1	Cross section of an LWT cask that transports four Spent PWR fuel assemblies	44
Figure 2	Two-dimensional computational domain of an LWT cask	45
Figure 3	Normal hot-day temperature contours of an LWT cask	46
Figure 4	Normal hot-day temperatures versus distance from center along the diagonal lines	47
Figure 5	Peak cladding and surface temperatures versus heat generation rates and difference between peak cladding temperatures using different fuel models and grids refinements	48
Figure 6	Temperature profiles along the walls of basket openings versus cord coordinate for Nitrogen and Helium at $Q = Q_C$	49
Figure 7	Peak cladding and surface temperature versus time for regulatory 30 minute fire duration	50
Figure 8	Peak cladding temperature versus time duration at initial peak cladding temperature, $T_{PC,I} = 400^\circ\text{C}$	51
Figure 9	Durations of concern for different fuel models and gases	52
Figure 10	Peak cladding temperature versus time duration at initial peak surface temperature, $T_{PS,I} = 85^\circ\text{C}$	53
Figure 11	Geometrically-Accurate isolated single fuel compartment model	54
Figure 12	Temperature dependent thermal conductivities for different materials used in 15x15 PWR isolated fuel compartment model	55

Figure 13	Effective thermal conductivity isolated fuel compartment model	56
Figure 14	Temperature contours of quarter geometry for Nitrogen at $T_{WALL} = 25^{\circ}\text{C}$ and $Q = 432.2 \text{ W}$	57
Figure 15	difference between max temperature and wall temperature versus distance from center along the diagonal line for Nitrogen at $T_{WALL} = 25^{\circ}\text{C}$ and $Q = 432.2 \text{ W}$	58
Figure 16	Difference between center temperature and wall temperature versus heat load at different wall temperatures	59
Figure 17	Ratio of difference between center temperature and wall temperatures versus heat load for HG and AG models	60
Figure 18	Dependence of Global effective thermal conductivity on heat load at different wall temperatures	61
Figure 19	Effective thermal conductivity versus wall temperature	62
Figure 20	Cross section of effective thermal conductivity truck cask	63
Figure 21	normal hot-day temperatures versus distance from center along the diagonal line for AG and HG models	64
Figure 22	Peak cladding and surface temperatures versus heat load for AG and HG models	65
Figure 23	Temperature profiles along the walls of basket openings versus cord coordinate for AG and HG models	66
Figure 24	Peak cladding temperature versus time duration for AG and HG models for regulatory 30 minute fire	67

- Figure 25** Peak cladding temperature versus time duration for HG model at initial peak cladding temperature, $T_{PC,I} = 400^{\circ}\text{C}$ 68
- Figure 26** Durations of concern for AG and HG models for two different initial conditions, $T_{PC,I} = 400^{\circ}\text{C}$ and $T_{PS,I} = 85^{\circ}\text{C}$ 69
- Figure 27** Peak cladding temperature versus time duration at initial peak surface temperature, $T_{PS,I} = 85^{\circ}\text{C}$ 70

NOMENCLATURE

PWR	Pressurized Water Reactor
BWR	Boiling Water Reactor
SNF	Spent Nuclear Fuel
LWT	Legal Weight Truck
CFD	Computational Fluid Dynamics
SCFD	Stagnant Gas Computational Fluid Dynamics
ETC	Effective Thermal Conductivity
Q	Heat Generation Rate within an individual fuel assembly
Q _C	Maximum allowable heat generation rate at which the fuel clad reaches its limit temperature
Q _S	Maximum allowable heat generation rate at which the package surface reaches its limit temperature
T _{AVG}	Average of the temperature along the walls of fuel basket
ΔT _{MAX}	Maximum Temperature difference in a basket
ΔT _C	Maximum Temperature difference between center and wall
T _{CLAD,MAX}	Temperature of cladding concern
T _{SURF,MAX}	Temperature of surface concern
T _{ENV}	Environmental Temperature
ε _{CLAD}	Cladding surface emissivity
ε _{FSS}	Support Structure surface emissivity
ε _{SS}	Stainless Steel emissivity
AG	Accurate Geometry

HG	Homogenized Geometry
He	Helium
N ₂	Nitrogen
T _{WALL}	Wall Temperature
k	Thermal Conductivity
k _U	Uniform effective thermal conductivity
k _H	Homogenized effective thermal conductivity
D	Duration
A	Area of the materials in the assembly
ρ	Density
C _P	Specific Heat Capacity
T	Temperature
NCT	Normal Conditions of Transport
HAC	Hypothetical Fire Accident Conditions
CD	Creep Deformation
BR	Burst Rupture
D _{CD}	Duration to reach creep deformation
D _{BR}	Duration to reach burst rupture
T _{PC}	Peak Cladding Temperature
T _{PS}	Peak Surface Temperature
T _{PC,I}	Peak cladding temperature for NCT and fire at time, t = 0
T _{PS,I}	Peak surface temperature at shaded conditions and fire at time, t = 0
d	Diameter of the package

Pr	Prandtl Number
Ra	Rayleigh Number
Nu	Nusselt Number
ν	Kinematic Viscosity
α	Gas Thermal Diffusivity
T_{LOCAL}	Local temperature
w	Distance from center along the diagonal line in 15x15 assembly
r	Radial Distance from center along the diagonal line in PWR assembly
s	Basket height in LWT cask package
L	Active length of the assembly

CHAPTER 1

INTRODUCTION

1. 1 Motivation

Light water reactor nuclear fuel assemblies consist of fuel rods held in square arrays by periodic spacer plates [1, 2, 3]. The rods themselves are stacks of UO_2 fuel pellets within zircaloy cladding. Some spaces in the array contain hollow instrumentation or guide thimble tubes instead of fuel rods. Different boiling water reactor (BWR) assemblies consist of 6×6 to 9×9 arrays of rods surrounded by a square-cross-section zircaloy channel. Pressurized water reactor (PWR) assemblies generally consist of 9×9 to 17×17 rod arrays but do not have surrounding channels. PWR rod diameters are generally smaller than those of BWRs, but their total assembly cross sections are larger.

Spent nuclear fuel (SNF) is placed in water pools after it is removed from a reactor to allow its heat generation and radioactive decay rates to decrease [4]. After an appropriate time SNF is placed in casks for dry storage or offsite transport [4, 5]. In transportation casks, individual SNF assemblies are supported horizontally within square cross-section basket tubes inside the cask's containment region. That region is evacuated and backfilled with helium or another non-oxidizing gas. Casks transported by truck or rail have enough space for roughly 4 or 21 PWR assemblies, respectively [5, 6].

Heat generated by the SNF assemblies makes the cask and fuel hotter than their surroundings. However, the zircaloy cladding that encapsulates the UO_2 pellets provides an important containment boundary. However, it may develop radial hydrides and become brittle if its temperature exceeds 400°C for extended periods [7]. The clad temperature must therefore be below 400°C during normal conditions of transport [8].

Federal regulations also require that cask surface temperature be below 85°C when it is in the shade [9] (this requirement may be avoided if a personnel barrier is used). Fuel cladding may experience creep deformation or burst rupture if its temperature exceeds 570°C or 750°C, respectively [7, 10]. It is therefore important that these temperatures be avoided even under fire accident conditions.

Cask operators must determine cask thermal dissipation capacity, Q_{TDC} . These are the fuel heat generation rates that cause either the peak fuel cladding temperature to reach 400°C (Q_C) during normal transport, or the surface temperature to reach 85°C (Q_S) in the shade. These capacities help operators determine how long the fuel must be aged underwater before it can be loaded into a dry cask. Transportation risk analysts also need to determine how long a transport cask can be in a fire before it reaches either 570°C or 750°C. These critical fire durations D_C helps analysts determine which fires have a potential to challenge the integrity of the cladding.

1.2 Background

Finite element thermal simulations are used to predict cask and fuel temperatures for a given fuel heat generation rate [5]. Multiple simulations are used to determine the maximum fuel heat generation rate that does not cause the fuel cladding to exceed its temperature limit [11]. The multiple fuel regions of a cask are complex to model because each contains many fuel rods. In the past computational resources were not available to perform multiple calculations in finite element models that accurately represented the fuel. To address this problem, the fuel assemblies and backfill gas were replaced by

fictitious but representative solid elements with temperature-dependent effective thermal conductivities (ETC) [2, 5, 12, 13,].

Manteufel and Todreas [13] developed ETC models based on a one-dimensional analytical model of radiation and conduction heat transfer in a two-dimensional array of heated rod within a stagnant gas. That model does not account for unheated tubes or channels, or multi-dimensional effects. Bahney and Lotz [2] performed two-dimensional finite element thermal simulations of several different fuel assemblies, including unheated components, within isothermal enclosures. They developed ETC models based on conduction and radiation heat transfer. In some cases ETC models are employed in analysis without stating their source or the methods used to develop them [5, 12].

A shortcoming of conductivity models is that they approximate heat flux at a location based only on the temperature and its spatial gradient at that location. This is not universally appropriate. Natural convection heat flux is dependent on local velocity, which depends on temperatures at different locations. Radiation heat transfer also depends on temperatures at a distance. As a result, a conductivity model that is appropriate within fuel basket openings near the center of a large rail cask, where the surface is nearly isothermal, may not be accurate for tubes near its periphery. Simulations have shown that the basket temperature near the periphery of rail cask is highly non-uniform [14]. This is important because the thermal resistance of the periphery cells strongly affect the temperature of the center basket opening, which affects the hottest cladding.

Homogenized fuel region models have been used to predict peak fuel cladding temperatures under normal conditions of transport in safety analysis reports used to

license transport casks [5]. They have also been used to estimate the thermal dissipation capacity of rail [11] and truck [15] transport casks. These works show that the surface temperature of basket compartments near the periphery of casks is highly non-uniform.

Homogenized fuel region models with effective conductivities have also been used to predict the peak cladding temperature during fire accident conditions [16, 17, 18]. However, to our knowledge, the accuracy of this approach for the high temperature and transient conditions that exist during and after a fire has not been evaluated.

The simplifying assumptions employed in ETC models are intended to over-predict the cladding temperature. Finite element cask models that employ this methodology therefore under-predict the cask thermal capacity. This can cause operators to under-load cask compared to their true safe capacity. This increases the required number of storage and transport casks, the number of shipments, and the associated costs. More accurate (less conservative) predictions of cask capacity can lead to lower system costs. It can also reduce the number of shipments and therefore the risk of transportation accidents.

Experiments that measure the temperature within mock fuel assemblies inside isothermal enclosures have provided a good understanding of the combined natural convection and radiation heat transfer within the fuel assemble/backfill gas regions of casks [19, 20, 21]. Computational fluid dynamics (CFD) simulations of those experiments accurately reproduced that data [22 - 25] and hold promise for developing improved fuel region heat transfer models.

1.3 Objective

Currently available computational resources are sufficient to perform two-dimensional simulations in a full cask cross section that employ CFD in the multiple fuel regions. This can lead to better estimates of the cask thermal capacity for specific fuel and cask designs, even for non-uniform fuel heat generation. It also provides an opportunity to accurately determine the non-isothermal temperature profiles of the periphery basket tubes [11].

In the current work two-dimensional models of a legal weight truck (LWT) cask cross-section are developed. Four PWR assemblies, each consisting of a 15x15 square array of heat generating fuel rods, are placed within the basket tubes. Buoyancy induced gas motion and Natural convective/radiation heat transfer within the fuel regions, as well as conjugate conduction in the solid regions, are modeled using the Fluent CFD package. The results are compared to those from finite element models that employ ETC models in the fuel regions.

The maximum allowed heat generation rate that causes the cladding to reach its temperature limit is determined for atmospheric pressure helium and nitrogen backfill gases. The sensitivity of the allowable heat generation rate to the cladding emissivity is also evaluated. The non-uniform temperature profiles of the basket tubes are determined at the maximum allowed heat generation rate. These profiles will be used in future benchmark experiments.

The objective is to describe the development of effective thermal conductivities for SNF assemblies as a methodology for performing future waste package thermal analyses. Finite element models of various SNF assembly types with fill environments of

helium or nitrogen have been developed and then used as the basis for the determination of effective thermal conductivities of assemblies with smeared (homogeneous) properties.

Effective thermal conductivities [13] are an alternative methodology for the prediction of SNF cladding temperatures. Cladding temperatures determined using derived effective thermal conductivities are compared to temperatures using other cladding temperature prediction methods (CFD and SCFD). The effective thermal conductivities developed here provide a method for predicting (with a high level of confidence) a "best estimate" of peak cladding temperatures for SNF assemblies in a dry environment.

The key to accurate SNF cladding temperature predictions using the effective thermal conductivity method lies in determining the proper conductivity to assume in the assembly volume. The peak cladding temperatures are a function of the assembly type, the assembly decay heat, and the basket wall temperature. It is important to note that the basket wall temperature not only specifies the environment temperature for the assembly, but it also impacts what portion of the decay heat will be transferred by thermal radiation which depends on the fourth power of the absolute temperatures (the higher the temperature, the more heat flows by radiation).

For an SNF assembly in a gaseous environment, Helium or Nitrogen backfill gases, heat will be transferred by gaseous conduction, convection, and radiation. The nonlinear temperature dependence for radiation heat transfer introduces severe nonlinearities into the otherwise linear heat transfer calculation. Therefore, any calculated effective thermal conductivity will be highly temperature-dependent (and nonlinear) and cannot be specified by just one value for a given assembly type.

To determine the appropriate effective thermal conductivity for a PWR assembly, detailed 2-D models of typical SNF assemblies were developed using the GAMBIT code including both gaseous heat transport and thermal radiation. An intact Babcock & Wilcox (B&W) 15x15 Mark B4 PWR [3] assembly was chosen as the basis for the 2-dimensional model of a 15x15 assembly which, using symmetry, represents one quarter of an assembly. The model includes the basket wall, 225 UO₂ fuel rods, Zircaloy cladding and Helium or Nitrogen backfill gases. Evaluating a variety of spent fuel characteristics and temperature levels, temperature and heat-load dependent effective thermal conductivities for homogeneous "smeared" assemblies were derived.

CHAPTER 2

COMPUTATIONAL MODELS

2.1 Legal Weight Truck package

Figure 1 shows the cross section of a generic Legal Weight Truck (LWT) cask loaded with four spent PWR fuel assemblies. This cask is similar but not identical to a currently licensed package [5]. The model is developed using MSC/Patran. The cross section in Fig. 1 is midway between cask ends. The dot-filled region represents four 15x15 PWR fuel assemblies within backfill gas. All 225 fuel rods of each assembly are identical. Each contains UO_2 pellets of diameter 9.36 mm enclosed in zircaloy cladding of thickness 0.78 mm. No gap or contact resistance between the pellets and cladding are modeled. The square tube array has center to center spacing of 14.5 mm, and the distance between the center of the outer most rod and the basket wall is 9.82 mm. The fuel assembly is similar to a Babcock & Wilcox 15x15 Mark B PWR [3], but the model does not contain unheated components.

The cross-shaped component at the center of the package is a 1.5 cm thick stainless steel support structure. Its surface emissivity is $\epsilon_{\text{FSS}} = 0.8$. Borated carbon (B_4C) pellets fill 1.1 cm-diameter holes that are drilled radially in the legs of the structure. The sides of the four square openings where the fuel is placed are $H = 22.3$ cm long.

The support structure and fuel are surrounded by a 0.96 cm thick stainless steel liner. Its emissivity is $\epsilon_{\text{SS}} = 0.2$. The liner is surrounded by a depleted uranium gamma shield. Its maximum thickness is 6.7 cm and it has an outer radius of curvature of 11.4 cm at its corners. A 3.8 cm thick stainless steel package body surrounds the gamma shield.

An external, 12.4-cm-thick neutron shield encircles the package. A single region is used to model several components. These components are 12.1-cm-thick Polypropylene-1% boron, 24 aluminum radial fins of thickness 0.245 cm, and a 0.27 cm thick stainless steel outer skin. The mixture thermal conductivity for this composite structure was developed based on an equivalent conduction model [27].

Heat generated within the fuel rods is transferred to the surrounding surfaces by natural convection and radiation heat transfer across the backfill gas, and conduction through the rod spacer plates. In this work we neglect the spacer plates.

2.2 Geometrically-Accurate Isolated Fuel Compartment Model

Figure 11 shows a two-dimensional cross-section model of a General Electric 15x15 PWR assembly constructed using the Fluent computational fluid dynamics package. This assembly is based on information presented by Bahney and Lotz [2]. The assembly consists of 225 fuel rods in a square array with 14.50 mm center-to-center spacing. Each rod consists of 9.36 mm diameter uranium dioxide (UO_2) fuel pellets contained in zircaloy cladding. The cladding outer diameter and wall thickness are 10.92 mm and 0.78 mm, respectively. The square channel outer dimension is 217.5 mm. The fuel pellets are assumed to be centered within the cladding and the assembly is centered within the basket.

Three sets of voids exist between the following pairs of solid components, the pellets and cladding, the cladding and channel, and the channel and basket. In this work conduction is modeled within all solid elements, and surface to surface radiation is modeled across all the voids. Different simulations are performed with atmospheric

pressure helium (He) or nitrogen (N₂) in these voids. Different simulations are performed that model either conduction or natural convection in the gas-filled regions.

Temperature dependent thermal conductivities are used for uranium dioxide, zircaloy, and helium and nitrogen gas [2]. The emissivity of stainless steel is set to $\varepsilon = 0.6$. For zircaloy, a base value of $\varepsilon = 0.806$ is used [2].

2.3 Effective Thermal Conductivity Isolated Compartment Model

Figure 13 shows a two dimensional cross section of a homogenized grid fuel region model constructed using Fluent computational dynamics package. The assembly consists of a homogeneous region instead of 225 fuel rods, zircaloy cladding and cover gases in a square array with 217.5 mm assembly height [2]. The homogeneous assembly consists of relatively small number of nodes and elements than a 15x15 PWR assembly.

2.4 Effective Thermal Conductivity Truck Package

Figure 20a shows the cross section of an effective thermal conductivity model of a Legal Weight Truck (LWT) cask. The UO₂ heater rods, zircaloy cladding and the cover gas are replaced by a homogeneous region with uniform volumetric heat generation rate and effective thermal conductivity equivalent to conduction and radiation heat transfer in the compartment confines. Figure 20b shows the temperature contour for effective thermal conductivity model while Figure 20c shows the temperature contour for geometrically-accurate model.

CHAPTER 3

COMPUTATIONAL METHODS

3.1 Legal Weight Truck package

Figure 2 shows the computational mesh of a LWT cask used in the current work. Only one half of the cask cross section is modeled to take advantage of the geometric and boundary condition symmetry. The computational grid was constructed using MSC Patran software. The dimensions are the same as those described for Figure 1. Mesh independence is evaluated using coarse and fine grids with 46,798 and 210,874 elements, respectively. Portions of the fuel region of those meshes are shown in Figs 2b and 2c. They show grid points within the fuel pellet, cladding and the cover-gas region. The majority of simulations presented in this work use the coarse grid.

The meshes in Figure 2 are imported into the Fluent CFD package. That code utilizes the finite volume method to solve the governing mass, momentum and energy equations. A second order upwind discretization scheme is used to solve the momentum and energy equations along with SIMPLEC algorithm for pressure velocity coupling. For the CFD simulations, Fluent calculates buoyancy induced gas motion, convection and surface-to-surface radiation heat transfer across the gas filled regions, and conduction in the solid components.

The current simulations calculate the cask and fuel temperatures using two different methods. The first uses CFD simulations that include buoyancy-induced fluid motion. The other uses CFD but assumes the gas speed is zero (Stagnant-CFD or SCFD). Both these models include the effects of radiation heat transfer across the gas-filled regions. Comparison of these two results shows the effect of gas motion.

Different simulations are performed for each model using Helium or Nitrogen cover gases. Temperature dependent thermal conductivities are applied to all solid and gas components. Those properties are obtained from standard sources [5, 6]. The support structure and stainless steel liner emissivities are $\epsilon_{\text{FSS}} = 0.8$ and $\epsilon_{\text{SS}} = 0.2$, respectively. The cladding emissivity used in the simulations is $\epsilon_{\text{C}} = 0.8$

For all calculations a uniform volumetric heat generation was applied to all the fuel pellets. It was determined by dividing the total heat generation rate of each assembly by the total volume of its fuel pellets (0.0495 m^3 , based on a rod length of 3.601 m [3]) multiplied by a peaking factor of 1.1351 [2]. By contrast Venigalla and Greiner [15] used a peaking factor of 1.25. The peaking factor accounts for the higher heat generation rate in the midsection of the PWR assembly compared to its average.

The steady state package temperatures were calculated for the regulatory normal transport environment [9]. These temperatures are used as initial conditions for a transient calculation that determines the time-dependent package temperatures during a fire. Finally, the package temperatures at the end of the fire are used as initial conditions for a post-fire cool down calculation.

3.2 Geometrically-Accurate Isolated Fuel Compartment Model

Figure 11 shows a two dimensional computational mesh of a 15X15 PWR assembly used in the current work. The computational grid was constructed with use of FLUENT software package. Mesh independence is evaluated using coarse, fine and finer grids with 86400, 183600 and 316800 elements, respectively. The majority of simulations presented in this work use the fine grid. Simulations are performed with uniform basket

wall temperatures of $T_w = 25\text{ }^\circ\text{C}$ to $T_w = 1000\text{ }^\circ\text{C}$ and fuel assembly heat generation rates of $Q = -3000$ to 3000 Watt. The volumetric heat generation rate within the pellets is determined by dividing the assembly generation rate by the total fuel pellet volume assuming that the cylindrical pellet volume in each rod is 3.601 m long [3]. The PWR model is initially run with only conduction and radiation present, using Helium and Nitrogen backfill. The heat generation rates are multiplied by a peaking factor of 1.1351 [2] to account for the higher heat generation at the axial center of the assembly. Therefore our 2D model is a section of the assembly that is at its axial center. The volumetric heat generation rate for the accurate geometry is calculated as,

$$q_{AG} = \frac{Q * P}{N^2 \frac{\pi}{4} d^2 L}$$

where, Q = Heat Load [W]

P = Peaking Factor, 1.1351

N = Number of rods in the assembly, 225

d = Diameter of the UO_2 rod [m]

L = Active length of the assembly [m]

Conduction and radiation temperature results are obtained by solving the steady state energy equation using a finite volume method with a second order discretization scheme. For natural convection/radiation simulations, the steady state conservation of momentum equations are solved with a second order upwind scheme, to obtain velocity and pressure fields.

Table 3 shows the material properties for UO₂ fuel rods, Zircaloy cladding and Helium and Nitrogen cover gases. The values of Density, Specific Heat Capacity and the area are listed in the table. Figure 12 shows the temperature dependent thermal conductivity values for UO₂ fuel rods, Zircaloy cladding, and Helium and Nitrogen cover gases.

3.3 Effective Thermal Conductivity Isolated Compartment

Figure 13 shows a two dimensional computational mesh of a homogeneous fuel region model used in the current work. The computational grid was constructed using GAMBIT software package. The meshes in the figure are imported into the Fluent CFD package. Mesh independence is evaluated using coarse and fine grids with 625 and 2500 elements, respectively. The majority of simulations presented in this work use the fine grid. Simulations are performed with uniform basket wall temperatures of $T_w = 25\text{ }^\circ\text{C}$ to $T_w = 1000\text{ }^\circ\text{C}$ and fuel assembly heat generation rates of $Q = -3000$ to 3000 Watt. The volumetric heat generation rate for effective thermal conductivity model is calculated as,

$$q_{HG} = \frac{\pi d^2 L}{4 H^2} * q_{AG}$$

where, H = Height of the assembly

q_{AG} = Volumetric Heat generation for Accurate Geometry

For a uniform boundary temperature at the wall and a uniform heat generation rate (defined in terms of the assembly decay heat load over the total axial length of the active fuel), the effective thermal conductivity can be expressed as,

$$k_{\text{eff}} = 0.073925 \frac{Q}{L(T_C - T_W)}$$

where Q = Total decay heat load in the assembly

L = Active length for the assembly

T_C = Center temperature in the assembly

T_W = uniform wall temperature.

3.4 Effective Thermal Conductivity Truck Package

Figure 20a shows the computational meshes used in the current work. Only one half of the cask cross section is modeled to take advantage of the geometric and boundary condition symmetry. The computational grid is constructed using MSC Patran software.

The ETC simulations are performed using the Fluent CFD code. In that model the region inside each square opening of the fuel basket is divided into a central square that represents the fuel assembly, and a thin edge region that represents the gas filled gap between the assembly and basket. For the current work the outer edge thickness is 0.3 cm [13], which is the distance between the outermost rod center and the wall, minus half the pin center-to-center pitch. The interior square with side length 217.5 mm represents the fuel.

A uniform volumetric heat generation rate is applied to the central square region. It is determined by dividing the total assembly heat generation rate by the effective fuel volume (area of the square region times its effective length), multiplied by a peaking factor.

3.5 Cask Boundary Conditions

3.5.1 Normal Conditions of Transport

Federal regulations require that cask temperatures be determined while the cask is subjected to Normal Conditions of Transportation [9]. Those conditions are still air at an environment temperature of $T_{ENV} = 38^{\circ}\text{C}$, with a constant, solar Heat Flux of 388 W/m^2 absorbed by the exterior package surface. In this work, the solar absorptivity is 0.57 and the package radiates to the environment with a surface emissivity of 0.2 [5]. The natural convection heat flux at each surface location is calculated as $q = h (T - T_{ENV})$. In this expression T is the local surface temperature, and h is the heat transfer coefficient between the package surface and its surroundings. It is determined based on a Nusselt number correlation for a horizontal cylinder in stagnant air [28]:

$$h = \frac{k}{d} \left(0.6 + \frac{0.387 * Ra^{1/6}}{\left\{ 1 + \left[\frac{0.559}{Pr} \right]^{9/16} \right\}^{8/27}} \right)^2 \quad (1)$$

In this equation the package diameter is $d = 2.42 \text{ m}$, k is the thermal conductivity of air, $Pr = \nu/\alpha$ is the Prandtl number. The kinematic viscosity of air is ν and thermal diffusivity is α . The Rayleigh number is,

$$Ra_d = \frac{g\beta(T - T_{ENV})d^3}{\nu\alpha} \quad (2)$$

where g is the acceleration of gravity and β is the isobaric expansion coefficient of air

3.5.2 Shaded Conditions

For this, the boundary conditions are the same as for the normal conditions of transport with still air at an environmental temperature of $T_{ENV} = 38^\circ\text{C}$ while the solar heat flux absorbed by the package exterior surface is set to zero.

3.5.3 Hypothetical Fire Accident Conditions

The Code of Federal Regulations [9] specifies a fire heat transfer model that can be used to evaluate transport cask under fire accident conditions. It consists of a fully-engulfing fire temperature and emissivity of at least 800°C and 0.9, and appropriate convection. For the current fire simulations, these lower limits are used along with a package surface emissivity of 0.8. For simplicity's sake, convection heat transfer between the fire and package is not included (The sensitivity of the results to convection may be considered in future work). The Code of Federal Regulations specify a fire duration of $D = 0.5$ hr. In the current work, we calculate the package response for a range of fire durations.

The package temperatures at the end of the fire (time $t = D$) are used as the initial condition for a transient post-fire calculation. In this work, the post-fire environment is identical to the normal hot day conditions of transport. These simulations calculate the temperatures throughout the package after the fire.

CHAPTER 4

SIMULATION RESULTS

4.1 Legal Weight Truck Package

4.1.1 *Normal Conditions of Transport*

Figure 3 shows the temperature contours in the right side of the cask for a fuel heat generation rate of $Q = 800$ W/assembly with N_2 cover gas. The plots in Figure 3a and 3b are from the CFD and SCFD simulations, respectively. The CFD simulation includes buoyancy-induced gas motion. As a result, the hottest location in each fuel compartment in Figure 3a is above the diagonal line passing through the cask center. The gas motion also causes the upper surface of the bottom cask to be hotter than the lower surface of the upper basket. As a result, heat transfers from the lower to the upper fuel region, making the upper region hotter than the lower. The hottest cladding is located in the upper opening and is 219°C . The SCFD simulations do not include gas motion. Their temperature contours are symmetric about the horizontal and diagonal lines that pass through the cask center. For SCFD simulations the maximum temperature is located on the diagonal and is 220°C .

Figure 4 shows temperature versus radial distance from the cask center s , for both CFD and SCFD fuel models. These temperatures are along the diagonal lines shown in Figure 3. Figure 4 shows results for both N_2 and He cover gases. For both gases (He & N_2) and models (CFD & SCFD), the temperature profiles are nearly identical outside the fuel/cover gas region ($s > 22.5$ cm). However the temperatures within the fuel regions are not the same. For N_2 , the SCFD model gives higher temperatures along the diagonal than the CFD model. Gas motion causes the difference. We note that the diagonal line passes

through the hottest fuel rod for SCFD model, but is below the hottest fuel rod for CFD model. For He, the temperature profiles from the CFD and SCFD are nearly identical. This is because the conductivity of the He is sufficiently high that gas motion does not affect heat transfer. The environmental temperature, $T_{ENV} = 38^{\circ}\text{C}$ is also shown. The external surface heat transfer coefficient and the solar heat flux used in this calculation significantly affect the temperature between the environment and cask surface. Future work will consider the sensitivity of the results to these quantities.

Figure 5a shows the peak cladding and peak surface temperatures versus heat generation rate as predicted by CFD and SCFD models. The peak cladding limit temperature, $T_{CLAD,MAX} = 400^{\circ}\text{C}$ and the peak surface limit temperature, $T_{SURF,MAX} = 85^{\circ}\text{C}$ is also shown. The lines marked with T_{PC} show the peak cladding temperature versus heat generation rate with solar heat flux. The lines marked with T_{PS} show the peak surface temperature versus heat generation rate when the solar heat flux is set to zero. Results from He and N_2 cover gases are presented. The CFD and SCFD results are so close together they are indistinguishable on this plot. For He, the peak cladding temperature reaches the clad limit temperature (400°C) at $Q = 3265 \text{ W/assembly}$ with CFD simulations. It is 30% lower when N_2 is the cover gas due to nitrogen's lower thermal conductivity. The values predicted by SCFD simulations are within 0.5% of those predicted by CFD calculations. The maximum cladding temperature without the solar heat flux is lower when He is the cover gas than for N_2 . The peak surface temperature is nearly the same for both He and N_2 cover gases for SCFD model. For CFD model, the peak surface temperature is slightly higher when N_2 is the cover gas than for He.

Table 1 shows the cask thermal dissipation capacity, Q_{TDC} that causes the cladding to reach the maximum limit temperature, $T_{CLAD, MAX} = 400^{\circ}C$. The CFD and SCFD models predict nearly the same Q_C values for both He and N_2 cover gases. This indicates that it may not be necessary to expend the computational resources required to calculate the fluid motion when calculating Q_C in future calculations.

Figure 5b shows the difference between peak cladding temperatures predicted by different models (CFD and SCFD) and grid refinements (Fine and Coarse). The lines labeled “He [Fine – Coarse]” and “ N_2 [Fine - Coarse]” shows the difference between SCFD simulations using the Fine and Coarse grids for He and N_2 cover gases, respectively. It shows that the maximum difference between the fine and coarse grid is $0.5^{\circ}C$ for He and $2.0^{\circ}C$ for N_2 . This difference is small compared to the difference between peak cladding temperature and surroundings. This indicates that the current simulations are mesh-independent. The other two lines show the difference between the SCFD and CFD results for He and N_2 cover gases. For N_2 cover gas, the SCFD calculations give slightly higher T_{PC} than the CFD simulations. This is expected because SCFD does not include fluid motion. For He, the CFD results are hotter than SCFD. However this difference is less than the difference between the fine and coarse grid results.

Figure 6 shows the basket wall temperatures versus wall coordinate, s . The plots show results for N_2 with $Q = Q_{C,N_2} = 2500$ W/assembly with SCFD model and $Q = Q_{C,N_2} = 2515$ W/assembly with CFD model, and He with $Q = Q_{C,He} = 3265$ W/assembly for both CFD and SCFD models. The s -coordinate is the distance along the basket surfaces in Figure 2. The value $s = 0$ corresponds to the corners closest to the package center, and

$s = 0.456$ is at the corner farthest from the location. Results from the two upper basket cords are presented. The walls close to the cask center are hotter and exhibit larger temperature gradients than the surfaces near the package periphery. For N_2 , the wall temperature varies from 213°C to 382°C for CFD and 190°C to 383°C for SCFD, while the variation for He is 209°C to 394°C for both CFD and SCFD. These results show that the compartment wall temperatures are highly non-isothermal.

Table 2 shows the cask thermal dissipation capacity, Q_S that causes the surface to reach the maximum limit temperature, $T_{\text{SURF, MAX}} = 85^\circ\text{C}$ without solar heat flux. For this case, the maximum cladding temperatures, $T_{\text{PC,I}}$ are different for both He and N_2 .

4.1.2 Hypothetical Fire Accident Conditions

4.1.2.1 Regulatory Duration Fire, $D = 0.5$ hr.

Figure 7 shows the peak cladding temperature response versus time in the upper fuel assembly for a regulatory 30-minute fire. A vertical dashed line shows the time at which the simulated fire ends and the post-fire conditions begin. The cladding temperatures begin to rise after the fire begins. They continue to rise after the fire is extinguished before peaking and then slowly decreasing. This delay is due to heat continuing to diffuse to the fuel from the hotter regions in the periphery of the cask.

In this figure, the upper two lines indicate the maximum cladding temperatures for an initial peak clad temperature of 400°C . The maximum temperature of the clad after the fire is extinguished is nearly the same for CFD and SCFD models for both cover gases. However, the maximum clad temperature is less than the creep deformation temperature of the clad, $T_{\text{CD}} = 570^\circ\text{C}$ in any of the models.

The bottom set of lines indicate the maximum cladding temperature when the initial surface temperature of the package is at 85°C. In this case, the peak clad temperature values are different for He and N₂ at time, $t = 0$.

4.1.2.2 Long Duration Fires, $0.5 \text{ hr} < D < 20 \text{ hr}$

Figure 8 shows Peak cladding temperature versus time duration for different fuel models and cover gases for different fire durations. The package temperature at the end of the fire (time, $t = D$) are used as the initial conditions for a transient post-fire calculations. In the current work, we calculate the package response for a range of fire durations, D . The post-fire environment is identical to the normal hot day transport conditions at an environment temperature of $T_{ENV} = 38^\circ\text{C}$ with a constant solar heat flux of 388 W/m^2 absorbed by the entire exterior package surface. These simulations calculate the temperatures throughout the package during and after the fire.

Figure 9 is a plot of the peak clad post fire temperature versus fire duration for both fuel models (CFD and SCD) and cover gases (He and N₂) for both the initial conditions, $T_{PC,I} = 400^\circ\text{C}$ and $T_{PS,I} = 85^\circ\text{C}$. Horizontal lines show two temperatures of concern for the cladding. The lower is the temperature limit for Creep Deformation, $T_{CD} = 570^\circ\text{C}$. The upper line is the temperature limit for Burst Rupture, $T_{BR} = 750^\circ\text{C}$. The durations of concern are the durations at which the peak cladding temperature curves in Figure 8 cross the horizontal lines for these temperatures.

Table 1 shows the durations of concern for clad to reach creep deformation and burst rupture temperatures with solar heat flux. The CFD and SCFD models predict

nearly the same creep deformation & burst rupture values for both He and N₂ cover gases.

Figure 10 shows the peak cladding temperature (without solar heat flux) versus time duration for different fuel models and cover gases for different fire durations. The initial cladding temperatures are different for Helium and Nitrogen cover gases. The package temperature at the end of the fire (time, $t = D$) are used as the initial conditions for a transient post-fire calculations. In the current work, we calculate the package response for a range of fire durations, D . These simulations calculate the temperatures throughout the package during and after the fire.

Table 2 shows the durations of concern for clad to reach creep deformation and burst rupture temperatures without solar heat flux. The CFD and SCFD models predict almost nearly the same creep deformation & burst rupture values for both cover gases.

4.2 Geometrically-Accurate Isolated Fuel Compartment Model

Figure 14a shows the temperature contours for the top right quarter geometry of the 15x15 PWR assembly model for a heat generation rate of $Q = 432$ W and wall temperature at $T_{WALL} = 25^{\circ}\text{C}$ for Nitrogen cover gas. The maximum temperature is located at the center of the assembly.

Figure 15 shows the difference between maximum temperature in the assembly and the wall temperature versus the distance from the center along the diagonal line shown in Figure 14 for Nitrogen cover gas at the wall temperature, $T_{WALL} = 25^{\circ}\text{C}$ and heat generation rate, $Q = 432$ watts for all the three models. All the three models give the

same temperature at the initial ($w = 0$ m) and end point ($w = 0.10875$ m) of the diagonal but not along it.

Figure 16 shows the difference between the center temperature of the assembly and the wall temperature versus heat generation rate for accurate geometry at different wall temperatures and heat generation rates for Helium and Nitrogen cover gases. The values shown are for the wall temperatures, $T_{WALL} = 25^{\circ}\text{C}$, 380°C and 1000°C and heat generation rate ranging from -3000 watts to 3000 watts. While ΔT_C increases with Q , the slope decreases at higher values of Q . This decrease in slope is a result of increased relative contribution from radiation heat transfer at higher temperatures. For each cover gas, the maximum temperature difference, ΔT_C is smaller for higher wall temperature than it is for lower wall temperature. This is once again due to the increased importance of radiation heat transfer at higher temperatures. Finally, for a given wall temperature, ΔT_C is smaller for Helium cover gas than it is for Nitrogen cover gas. This is caused by Helium's larger thermal conductivity.

4.3 Effective Thermal Conductivity Isolated Fuel Compartment Model

Figure 14b shows the temperature contours for a uniform Effective Thermal Conductivity model, $k_U(T_{WALL}, Q)$ with the same heat generation rate, wall temperature and cover gas for Figure 14a. At low wall temperatures and heat generation rates, the uniform thermal conductivity model gives almost the same results as the accurate geometry.

Figure 15 shows the difference between maximum temperature in the assembly and the wall temperature versus the distance from the center along the diagonal line

shown in Figure 14 for Nitrogen cover gas at the wall temperature, $T_{WALL} = 25^{\circ}\text{C}$ and heat generation rate, $Q = 432$ watts. Geometrically-accurate and the uniform effective thermal conductivity models give the same temperature at the initial ($w = 0$ m) and end point ($w = 0.10875$ m) of the diagonal but not along it.

Figure 12 shows the effective thermal conductivity values calculated from the above given equation versus temperature ranging from 25°C to 1000°C . The lines marked HG-Helium and HG-Nitrogen are calculated from the simulations performed on Geometrically-Accurate Isolated single fuel compartment model. These values are less than the thermal conductivity values for UO_2 rods and Zircaloy cladding but are more than the Helium and Nitrogen cover gases.

Figure 14c shows the temperature contours for an Effective Thermal Conductivity model, $k_H(T, Q = 0)$ with the same heat generation rate, wall temperature and cover gas for Figure 14a and 14b. At low wall temperatures and heat generation rates, all the three models give almost the same results.

Figure 15 shows the difference between maximum temperature in the assembly and the wall temperature versus the distance from the center along the diagonal line shown in Figure 14 for Nitrogen cover gas at the wall temperature, $T_{WALL} = 25^{\circ}\text{C}$ and heat generation rate, $Q = 432$ watts. All the three models give the same temperature at the initial ($w = 0$ m) and end point ($w = 0.10875$ m) of the diagonal but not along it. Effective thermal conductivity model, $k_H(T, Q = 0)$ gives a better temperature profile than for the uniform thermal conductivity model, $k_U(T_{WALL}, Q)$.

Figure 17 shows the ratio of temperature difference between center and wall versus heat generation rate for Homogenized geometry and Accurate Geometry for both

Helium and Nitrogen cover gases at different wall temperatures ranging from $T_{WALL} = 25^{\circ}\text{C}$ and $T_{WALL} = 1000^{\circ}\text{C}$. The ratio is close to 1 stating that the temperatures values calculated from effective thermal conductivity model are in agreement with the accurate geometry model.

Figure 18 shows the thermal conductivity values versus heat generation rate for different wall temperatures ranging from $T_{WALL} = 25^{\circ}\text{C}$ to $T_{WALL} = 1000^{\circ}\text{C}$ for Helium and Nitrogen cover gases. The Angular Discretization value of 8 is used for these calculations. The thermal conductivity values are lower when Nitrogen is the cover gas due to Nitrogen's higher temperature between center and wall.

Figure 19 shows the dependence of global Effective Thermal Conductivity values on uniform local temperatures for Helium and Nitrogen cover gases. The local temperature values ranges from 25°C to 1000°C . The values of Effective Thermal Conductivity, k are calculated assuming there is no heat generation rate in the assembly. These values are obtained from Figure 18 at heat generation rate, $Q = 0$ watts. These values are used as boundary conditions for Effective thermal Conductivity Truck package model.

4.4 Effective Thermal Conductivity Truck Package

4.4.1 Normal Conditions of Transport

Figure 21 shows the temperature versus radial distance from the cask center, r for both geometrically-accurate and effective thermal conductivity model. These temperatures are along the diagonal line shown in Figure 20. Figure 21 shows results for both Nitrogen and Helium cover gases. For gases (He & N_2) and models (geometrically-accurate & effective thermal conductivity), the temperature profiles are nearly identical

outside the cover gas region ($r > 0.225$ m). However the temperatures within the compartment region are not the same. For Nitrogen, the effective thermal conductivity model gives higher temperature along the diagonal than for geometrically-accurate model. The effective thermal conductivity model gives lower temperature along the diagonal than for geometrically-accurate model for Helium cover gas.

Figure 22 shows the peak cladding temperature, T_{PC} (with solar heat flux) and peak surface temperature, T_{PS} (without solar heat flux) versus heat generation rate as predicted by geometrically-accurate and effective thermal conductivity models. Results from Helium and Nitrogen cover gases are presented. For Helium, the peak cladding temperature reaches the clad limit at $Q = Q_{C,He} = 3647$ W/assembly for effective thermal conductivity model and is 11% higher than geometrically-accurate model. For Nitrogen, the values are $Q = Q_{C,N2} = 3046$ W/assembly and 21%, respectively. The peak surface temperatures are nearly the same for both the cover gases for geometrically-accurate and effective thermal conductivity models. The maximum surface temperatures reach its maximum limit at $Q_S = 1000$ W/assembly for Effective thermal conductivity models and is 4% lower than the geometrically-accurate model. The peak cladding limit temperature $T_{CLAD, MAX} = 400^\circ\text{C}$ and peak surface limit temperature $T_{SURF, MAX} = 85^\circ\text{C}$ is also shown.

Table 4 shows the cask thermal dissipation capacity, Q_C that causes the cladding to reach the maximum limit temperature, $T_{CLAD, MAX} = 400^\circ\text{C}$ for geometrically-accurate, AG and effective thermal conductivity, HG models. For both helium and Nitrogen cover gases, the Q_C values for effective thermal conductivity model are higher than the geometrically-accurate model. This shows that the effective thermal conductivity models are non-conservative for predicting the peak cladding temperatures.

Table 5 shows the cask thermal dissipation capacity, Q_S that causes the surface to reach the maximum limit temperature, $T_{SURF, MAX} = 85^\circ\text{C}$ without solar heat flux for both cover gases and models. For this case, the maximum cladding temperatures are different for both the cover gases and models. For both helium and Nitrogen cover gases, the Q_S values for effective thermal conductivity model are lower than the geometrically-accurate model. This shows that the effective thermal conductivity models are conservative for predicting the peak surface temperatures.

Figure 23 shows the compartment wall temperatures versus wall coordinate, s . The plots show results for Nitrogen with $Q = Q_{C,N_2} = 2500$ W/assembly for geometrically-accurate and $Q = Q_{C,N_2} = 3046$ W/assembly for effective thermal conductivity model and Helium with $Q = Q_{C,He} = 3265$ W/assembly for geometrically-accurate and $Q = Q_{C,He} = 3647$ W/assembly for effective thermal conductivity model. The s -coordinate is the distance along the compartment surface in Figure 20. Results from the upper compartment are presented. The walls close to the cask center are hotter and exhibit larger temperature gradients than the surfaces near the package periphery.

4.4.2 Hypothetical Accident Conditions

4.4.2.1 Regulatory Duration Fire, $D = 0.5$ hr.

Figure 24 shows the temperature response versus time of the fuel cladding in the upper fuel assembly in Figure 20 for regulatory 30 minute fire duration for both the models (Geometrically-accurate and Effective Thermal Conductivity) with and without solar heat flux and cover gases (He & N₂). A vertical dashed line shows the time at which the simulated fire ends and the post fire conditions begin. The cladding temperatures continue to rise after the fire is extinguished before peaking and then slowly decreasing.

The maximum cladding temperature for Helium cover gas with geometrically-accurate model is $T_{PC,PF} = 441^{\circ}\text{C}$ and for Nitrogen, it is $T_{PC,PF} = 433^{\circ}\text{C}$ where as for Effective Thermal Conductivity model, the maximum values for cladding are $T_{PC,PF} = 441^{\circ}\text{C}$ and $T_{PC,PF} = 435^{\circ}\text{C}$, respectively. The cladding temperature reaches its maximum in less time for both the cover gases for effective thermal conductivity model than for geometrically-accurate model. However, the peak cladding temperature is less than the creep deformation temperature of the clad, $T_{CD} = 570^{\circ}\text{C}$ in any of the models.

4.4.2.2 Long Duration Fires, $0.5 \text{ hr} < D < 20 \text{ hr}$

Figure 25 shows the peak cladding temperature (with solar heat flux) versus time duration for both the cover gases using effective thermal conductivity model at different fire durations. The package temperature at the end of fire (time, $t = D$) is used as the initial conditions for transient post-fire calculations. In the current work, we calculate the package response for a range of fire durations. The post-fire environment is identical to the normal hot day transport conditions. The same sets of simulations were run for geometrically-accurate models with Helium and Nitrogen cover gases for the same fire durations. The fire lasts for longer before reaching the critical durations of concern, D_C for geometrically-accurate model for both the cover gases.

Figure 26 summarizes the peak clad post fire temperatures for both fuel models (geometrically-accurate (AG) and effective thermal conductivity (HG)) and cover gases (He & N₂) with and without solar heat flux. Horizontal lines show the two temperatures of concern for the cladding. The effective thermal conductivity model predicts higher

temperatures than the geometrically-accurate model for both Helium and Nitrogen cover gases.

Figure 27 shows the peak cladding temperature at $T_{PS,I} = 85^{\circ}\text{C}$ (without solar heat flux) versus time duration for both the cover gases using effective thermal conductivity model at different fire durations. The package temperature at the end of fire (time, $t = D$) is used as the initial conditions for transient post-fire calculations. The initial cladding temperatures at time, $t = 0$ are different for both Helium and Nitrogen cover gases.

CHAPTER 5

SUMMARY AND CONCLUSIONS

This work assesses the temperature and resulting containment integrity of the fuel cladding within a generic legal weight truck package during normal conditions of transport and regulatory format fires using geometrically-accurate and homogenized fuel region models. The package studied in this work resembles a modern cask designed to transport four Pressurized Water Reactor fuel assemblies. This work uses a two-dimensional finite volume mesh that accurately represents the geometry of the cask, including the fuel inside. Computational Fluid Dynamic (CFD) simulations are performed that calculate buoyancy-driven gas motion, as well as the natural convection and radiation heat transfer in the gas filled fuel regions. These results are compared to Stagnant-gas CFD (SCFD) simulations, where the gas speed is set to zero, to evaluate the effect of gas motion.

During Normal Conditions of Transport, the fuel cladding temperature must not exceed 400°C to avoid the formation of radial hydrides. The Thermal Dissipation Capacity based on the cladding temperature, Q_C is the maximum allowable heat generation rate that causes the fuel clad to reach this temperature. The current CFD simulations predict that $Q_C = 3265$ W/assembly when He is the cover gas. It is 30% lower when N_2 is the cover gas due to Nitrogen's lower thermal conductivity. The values predicted by SCFD simulations are within 0.5% of those predicted by CFD calculations. This indicates that buoyancy-induced gas motion does not significantly affect the cladding temperature under these conditions, and less computationally-intensive SCFD simulations are sufficiently accurate to predict cladding temperatures.

Federal regulations also require that the cask surface temperature be below 85°C when the cask is in the shade. The fuel thermal dissipation capacity based on the surface temperature, $Q_S = 1040$ W/assembly with SCFD simulations for either N₂ or He cover gas. CFD simulations results are with 0.3 % of this value.

During a fire, the cladding may experience creep deformation or burst rupture if its temperature exceeds 570°C or 750°C, respectively. If the peak cladding temperature before a fire is 400°C, ($T_{PC,I} = 400^\circ\text{C}$) CFD simulations predict that the minimum durations of a regulatory format fire capable of bringing the cladding to 570°C or 750°C (critical fire durations) are $D_{CD} = 2.7$ hr and $D_{BR} = 7.2$ hr, respectively, when He is the cover gas. When N₂ is the cover gas, the critical fire durations are 22 and 15% longer. This longer duration is caused by the lower fuel heat generation rate when N₂ is the cover gas.

If the fuel heat generation is chosen so that the peak surface temperature is 85°C before the fire starts, ($T_{PS,I} = 85^\circ\text{C}$) then the critical fire durations for creep deformation and burst rupture are $D_{CD} = 4.7$ hr and $D_{BR} = 11.6$ hr, when He or N₂ are the respective cover gases. The values predicted by SCFD calculations are within 0.2% of those predicted by CFD simulations.

Homogeneous region fuel assemblies are developed with Effective thermal properties for a single assembly isolated fuel compartment with uniform temperature boundary conditions and assuming only radiation and conduction heat transfer. Effective Thermal Conductivity (ETC) simulations predict that $Q_C = 3647$ W/assembly when He is the cover gas. It is 19% lower when N₂ is the cover gas. The values predicted by ETC simulations are 11% and 21% higher for Helium and Nitrogen, respectively, compared to

those predicted by SCFD calculations. They also predict that $Q_s = 1000$ W/assembly when either Helium or Nitrogen is the cover gas. These values are within 4% of those predicted by SCFD simulations.

ETC simulations predict that the minimum durations of a regulatory format fire capable of bringing the cladding to 570°C or 750°C are $D_{\text{CD}} = 2.7$ hr and $D_{\text{BR}} = 6.8$ hr, respectively, when He is the cover gas. When N_2 is the cover gas, the critical fire durations are 11 and 7.3% longer. This longer duration is caused by the lower fuel heat generation rate when N_2 is the cover gas. If the surface temperature is 85°C before the fire starts, then the critical fire durations for creep deformation and burst rupture are $D_{\text{CD}} = 4.7$ hr and $D_{\text{BR}} = 11.6$ hr, respectively, when either He or N_2 are the cover gases. The values predicted by ETC calculations are within 4% of those predicted by SCFD simulations.

The effective thermal conductivity model shows that it is non-conservative method of estimating the cladding temperatures and fire durations when heat generation rate is chosen based on the initial cladding temperature of $T_{\text{PC,I}} = 400^\circ\text{C}$ for normal conditions of transport and Hypothetical fire accident conditions. It also shows that this model is conservative when heat generation rate is chosen based on the peak surface temperature of $T_{\text{PS,I}} = 85^\circ\text{C}$ for shaded conditions of transportation. This model provides an effective means of representing fuel assemblies in large CFD or FEA cask models with a relatively small number of nodes and elements.

CHAPTER 6

FUTURE WORK

The Full CFD simulations can be extended to study the natural convection/radiation heat transfer in other widely used configurations of PWR fuel assemblies such as 14X14 and 17x17. The simulation results must be benchmarked against experimental measurements before they can be used with confidence to design transport casks. Simulations similar to the ones performed in the current work for a truck cask can also be performed for much larger rail casks.

The assumed solar heat flux and external heat transfer coefficient values greatly affect the temperature response from the truck package. Future simulations may monitor the sensitivity of temperatures to these assumed values. Effective Thermal Conductivities are calculated for an isolated fuel compartment model with uniform wall temperature and applied to an assembly with non-uniform wall temperatures. In the future, ETC's can be calculated for isolated fuel compartment region with non-uniform wall temperatures.

REFERENCES

1. U.S Department of Energy, 1987, “*Characteristics of Spent Nuclear Fuel, High-Level Waste, and Other Radioactive Wastes Which May Require Long-Term Isolation*”, Office of Civilian Radioactive Waste Management, DOE/RW-0184.
2. Bahney, R.H., and Lotz, T.L., 1996, “*Spent Nuclear Fuel Effective Thermal Conductivity Report*,” prepared for the U.S. DOE, Yucca Mountain Site Characterization Project Office by TRW Environmental Safety Systems, Inc., D.I.: BBA000000-01717-5705-00010 REV 00.
3. Office of Civilian Radioactive Waste Management, 1987, “*Characteristics of Spent Fuel, High-Level Waste and Other Radioactive Wastes which may require Long-Term Isolation*,” Vol. 3, DOE/RW-0184, December.
4. Saling, J.H. and Fentiman, A.W., 2001, *Radioactive Waste Management*, 2nd Edition, Taylor and Francis, New York.
5. General Atomics (GA), 1998, “*GA-4 Legal Weight Truck From-Reactor Spent Fuel Shipping Cask, Safety Analysis Report for Packaging (SARP)*,” San Diego, California 92186-5608.
6. Office of Civilian Radioactive Waste Management (OCRWM), US Department of Energy, 1993, “*Multi-Purpose Canister (MPC) Implementation Program Conceptual Design Phase Report*,” DOC ID: A20000000-00811.
7. Johnson, A.B. and Gilbert, E.R., September 1983, “*Technical Basis for Storage of Zircaloy-Clad spent Fuel in Inert Gases*,” PNL-4835, Pacific Northwest Laboratory, Richland, Washington.

8. Nuclear Regulatory Commission (NRC), 2005, "*Cladding Considerations for the Transportation and Storage of Spent Fuel*", Interim Staff Guidance Report for the Spent Fuel Project Office of the U.S., ISG-11 Rev. 3, available at www.nrc.gov
9. U.S. Nuclear Regulatory Commission, 2002, "*Packaging and Transportation of Radioactive Material*," Rules and Regulations, Title 10, Part 71, Code of Federal Regulations, April.
10. Sprung, J.L., Ammerman, D.J., Breivik, N.L., Dukart R.J. and Kanipe, F.L., March 2000, "*Reexamination of Spent Fuel Shipment Risk Estimates*," NUREG/CR-6672, Vol.1 (SAND2000-0234), Sandia National Laboratories, Albuquerque, New Mexico.
11. Unterzuber, R., Milnes, R.D., Marinkovich, B.A. and Kubancsek, G.M., 1982, "*Spent-Fuel Dry-Storage Testing at EMAD (March 1978 through March 1982)*," Prepared for the US DOE Commercial Spent Fuel Management Program Office at the Pacific Northwest Laboratory, B-D3339-A-G.
12. Manteufel, R.D., and Todreas, N.E., 1994, "*Effective thermal conductivity and edge conductance model for a spent fuel assembly*," Nuclear Technology, Vol. 105, pp. 421-440.
13. Greiner, M., Gangadharan, K.K., and Gudipati, M., 2007, "*Use of Fuel Assembly/Backfill Gas Effective Thermal Conductivity Models to Predict Basket and Fuel Cladding Temperatures within a Rail Package During Normal Transport*," Nuclear Technology. Vol. 160, pp. 325-336
14. Greiner, M., Shin, S, Faulkner, R.J., and Wirtz, R.A., 1998a, "*Transport Cask Response to Regulatory Format Thermal Events, Part 1: Rail Package*," International J. of Radioactive Material Transport, Vol. 9, n 3, pp. 187–192.

15. Greiner, M., Faulkner, R.J., and Jin, Y.Y., 1998b, "*Transport Cask Response to Regulatory Format Thermal Events, Part 2: Truck Cask*," International J. of Radioactive Material Transport, Vol. 9, n 3, pp. 193–198.
16. Adkins, H.E. Jr., Cuta, J.M., Koepfel, B.J., Guzman, A.D., and Bajwa, C.S., 2006, "*Spent Fuel Transportation Package Response to the Baltimore Tunnel Fire Scenario*," NUREG/CR-6886, Rev. 1, PNNL-15313, Pacific Northwest National Laboratory.
17. Gudipati, M., and Greiner, M., 2007, "*CFD Simulations of Fuel Cladding and Basket Surface Temperatures in an MPC Rail Cask during Normal Transport*," Proceedings of the 15th International Symposium on the Packaging and Transportation of Radioactive Materials (PATRAM).
18. Mallidi, N., Greiner, M., and Venigalla, V.V.R., 2006, "*Fire Durations of Concern for a Modern Legal Weight Truck Cask*," PVP2006-ICPVT-11-93748, Proceedings of ASME Pressure Vessels and Piping Division Conference, July 23-27, Vancouver, BC, Canada.
19. Incropera, F.P., and DeWitt, D.P., 1996, *Introduction to Heat Transfer*, 3rd edition, J. Wiley and sons, New York.
20. Kakac, S., and Yener, Y., 1993, "*Heat Conduction, Third Edition*," Taylor & Francis, Bristol, PA.
21. Canaan, R. E. and Klein, D. E., 1996, "*An Experimental Investigation of Natural Convection Heat Transfer within Horizontal Spent Fuel Assemblies*," Nuclear Technology, Vol.116, pp. 306-318, December.

22. Office of Civilian Radioactive Waste Management (OCRWM), US Department of Energy, 1993, "*Multi-Purpose Canister (MPC) Implementation Program Conceptual Design Phase Report,*" DOC ID: A20000000-00811.
23. Gangadharan, K.K. 2006, "*Use Of Fuel Assembly/Backfill Gas Effective Thermal Conductivity Models to Predict Basket and Fuel Cladding Temperatures within a Rail Package during Normal Transport,*" Masters Thesis, Mechanical Engineering Department, University of Nevada, Reno.
24. Venigalla, V.V.R. 2007, "*Computational Fluid Dynamic Simulations of Natural Convection/Radiation Heat Transfer within the Fuel Regions of a Truck Cask for Normal Transport,*" Masters Thesis, Mechanical Engineering Department, University of Nevada, Reno.
25. Lovett, P. M., 1991 "*An Experiment to Simulate the Heat Transfer Properties of a Dry, Horizontal Spent Nuclear Fuel Assembly,*" M.S. Thesis, Nuclear Eng., Massachusetts Institute of Technology.
26. Arya, M. S. and Keyhani, M., 1990, "*Convective Heat Transfer in a Sealed Storage Cask Containing Spent Fuel Canisters,*" Journal of Nuclear Science and Engineering, Vol. 105, pp. 248-259.
27. Wix, S.D. and Koski, J.A., 1993, "*Numerically predicting horizontally oriented spent fuel rod surface temperatures,*" High level radioactive waste management: proceedings of the 4th annual international conference, Las Vegas, Nevada, April 26-30, pp. 1785-1789.

Cover Gas	Q_C [W]		D_{CD} [hr]		D_{BR} [hr]	
	CFD	SCFD	CFD	SCFD	CFD	SCFD
Helium	3265	3265	2.7	2.7	7.2	7.2
Nitrogen	2515	2500	3.3	3.3	8.38	8.39

Table 1: Heat Generation Rate and durations of concern for two different fuel models (CFD and SCFD) for $Q = Q_C$ for He and N_2 Cover gases at initial peak clad temperature, $T_{PC,I} = 400^\circ\text{C}$

Cover Gas	Q_s [W]		$T_{PC,I}$ [$^{\circ}$ C]		D_{CD} [hr]		D_{BR} [hr]	
	CFD	SCFD	CFD	SCFD	CFD	SCFD	CFD	SCFD
Helium	1040	1040	186	186	4.7	4.7	11.6	11.6
Nitrogen	1010	1040	222	237	4.9	4.8	11.8	11.7

Table 2: Heat generation rate and durations of concern for different fuel models (CFD and SCFD) and cover gases (Helium and Nitrogen) at initial peak surface temperature, $T_{PS,I} = 85^{\circ}$ C

	A	ρ	C_p
	[m²]	[kg/m³]	[J/kg-K]
Helium	0.026	0.164	5193
Nitrogen	0.026	1.138	1039
Zircaloy	0.005	6500	330
UO₂	0.015	10970	247
HG - Helium	0.047	4362	261
HG - Nitrogen	0.047	4362	261

Table 3: Material Properties used in the geometrically accurate and homogenized geometry isolated fuel compartment models

Cover Gas	Q_C [W]		D_{CD} [hr]		D_{BR} [hr]	
	HG	AG	HG	AG	HG	AG
Helium	3647	3265	2.7	2.7	6.8	7.2
Nitrogen	3046	2500	3.0	3.3	7.3	8.3

Table 4: Heat Generation Rates and Durations of Concern for $Q = Q_C$ ($T_{PC,I} = 400^\circ\text{C}$) for He and N_2 cover gases for different Fuel Models (Accurate Grid and Homogenized Grid).

Cover Gas	Q_s [W]		$T_{PC,I}$ [°C]		D_{CD} [hr]		D_{BR} [hr]	
	HG	AG	HG	AG	HG	AG	HG	AG
Helium	1000	1040	172	186	4.6	4.7	11.6	11.6
Nitrogen	1000	1040	203	237	4.6	4.8	11.6	11.7

Table 5: Heat Generation Rates and Durations of Concern for $Q = Q_C$ ($T_{PS,I} = 85^\circ\text{C}$) for He and N_2 cover gases for different Fuel Models (Accurate Grid and Homogenized Grid).

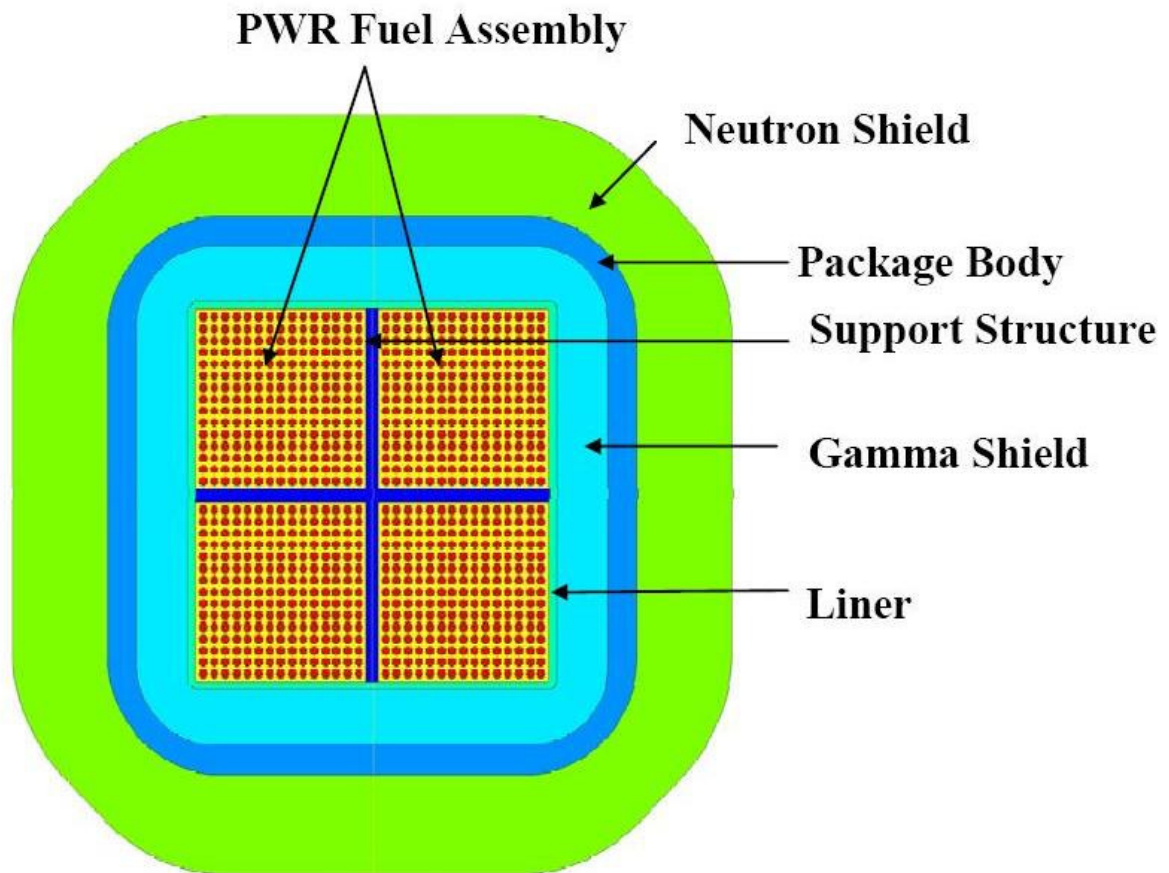


Figure 1: Cross section of an LWT cask that transports four Spent PWR fuel assemblies.

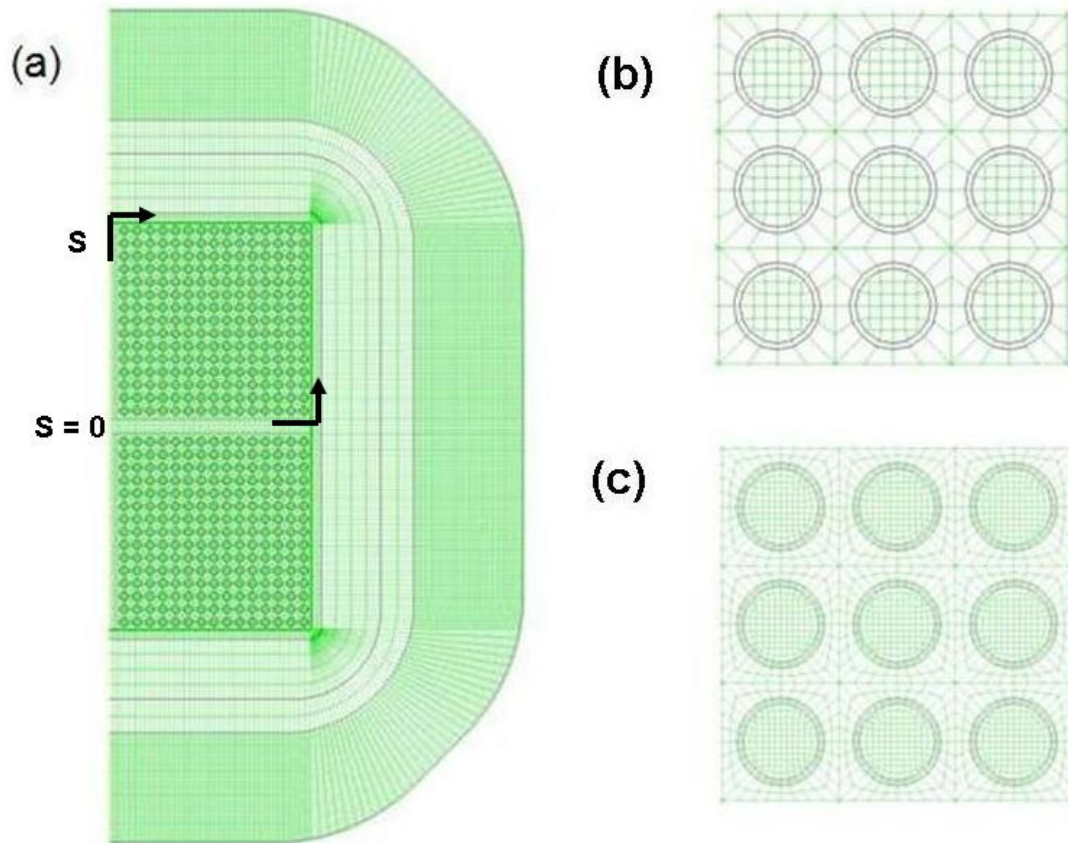


Figure 2: Two-dimensional computational domain of an LWT cask: (a) half cask coarse grid, (b) Detail of Coarse Grid with 46798 elements, and (c) Detail of Fine grid with 210874 elements.

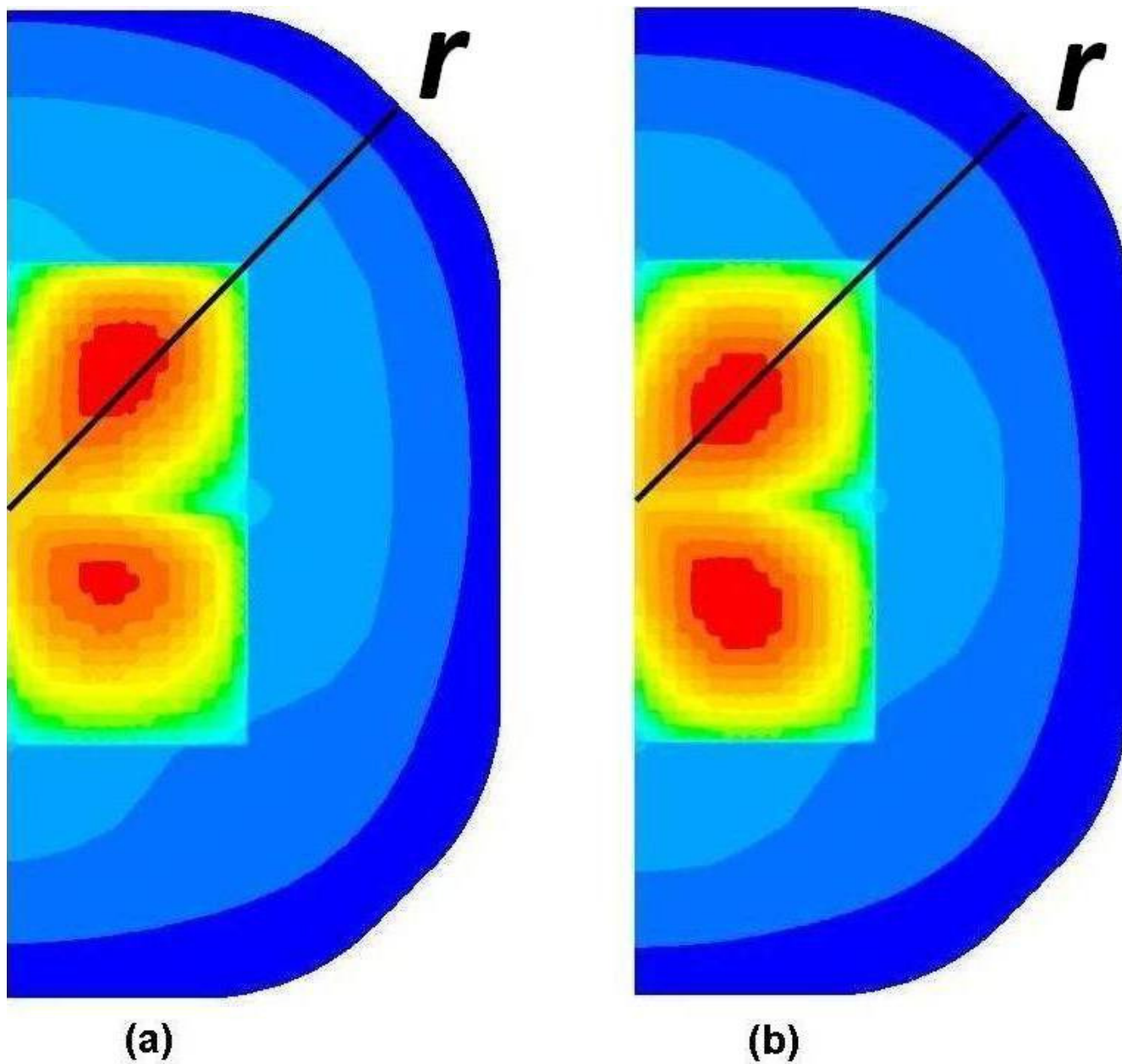


Figure 3: Normal hot-day temperature contours of an LWT cask for $Q = 800$ W/assembly with N_2 from two fuel region models: (a) CFD, (b) S-CFD.

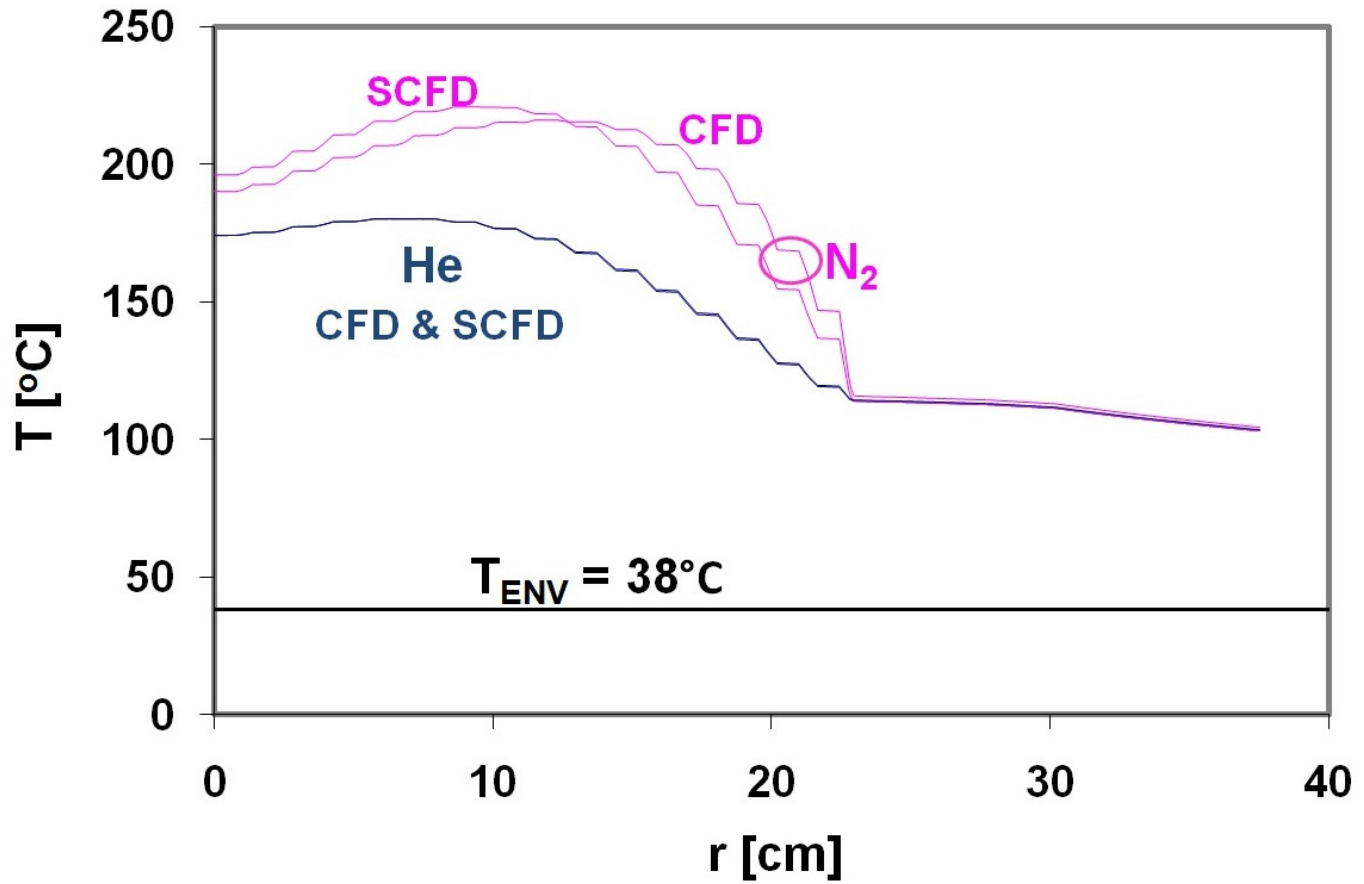
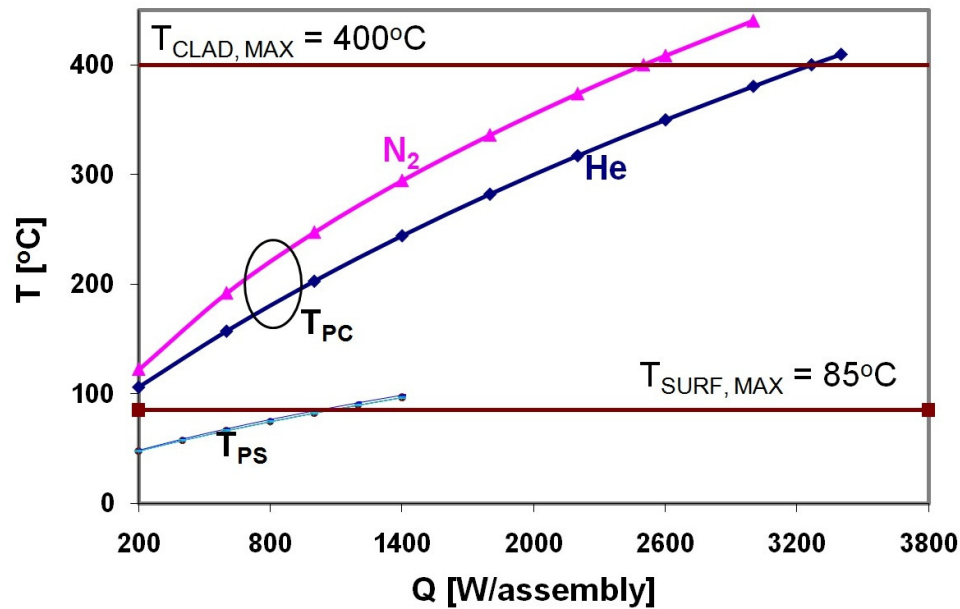
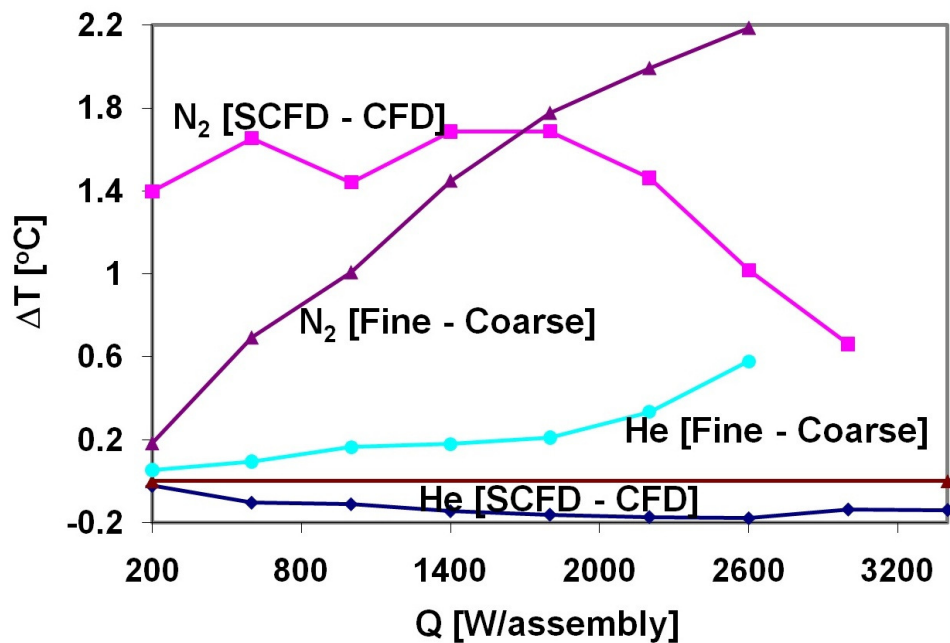


Figure 4: Normal hot day temperature versus distance from center along the diagonal lines in Figure 3 for $Q = 800$ W/assembly. The environment temperature is also shown.



(a)



(b)

Figure 5: (a) Peak Cladding temperature (with Solar Heat Flux) and Peak Surface temperature (without Solar Heat Flux) versus heat generation rate for different fuel models (CFD & SCFD) and cover gases (He & N_2). The fuel clad temperature and surface temperature limits are also shown. (b) Difference between peak cladding temperatures calculated using different fuel models and different grid refinements (Coarse & Fine).

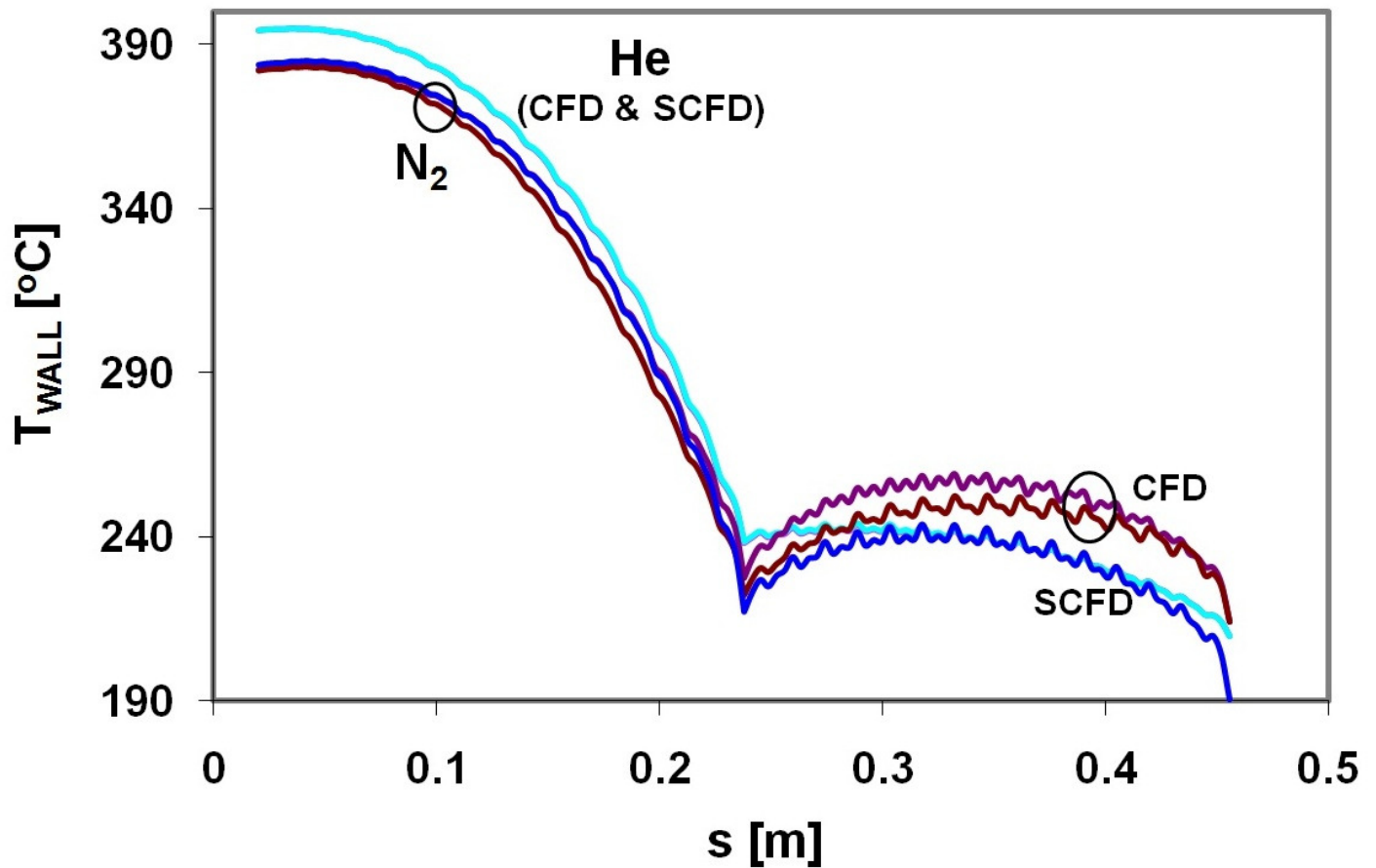


Figure 6: Temperature profiles along walls of basket openings versus cord coordinate for N_2 at $Q = Q_{C,N_2} = 2500$ W/assembly and He at $Q = Q_{C,He} = 3265$ W/assembly

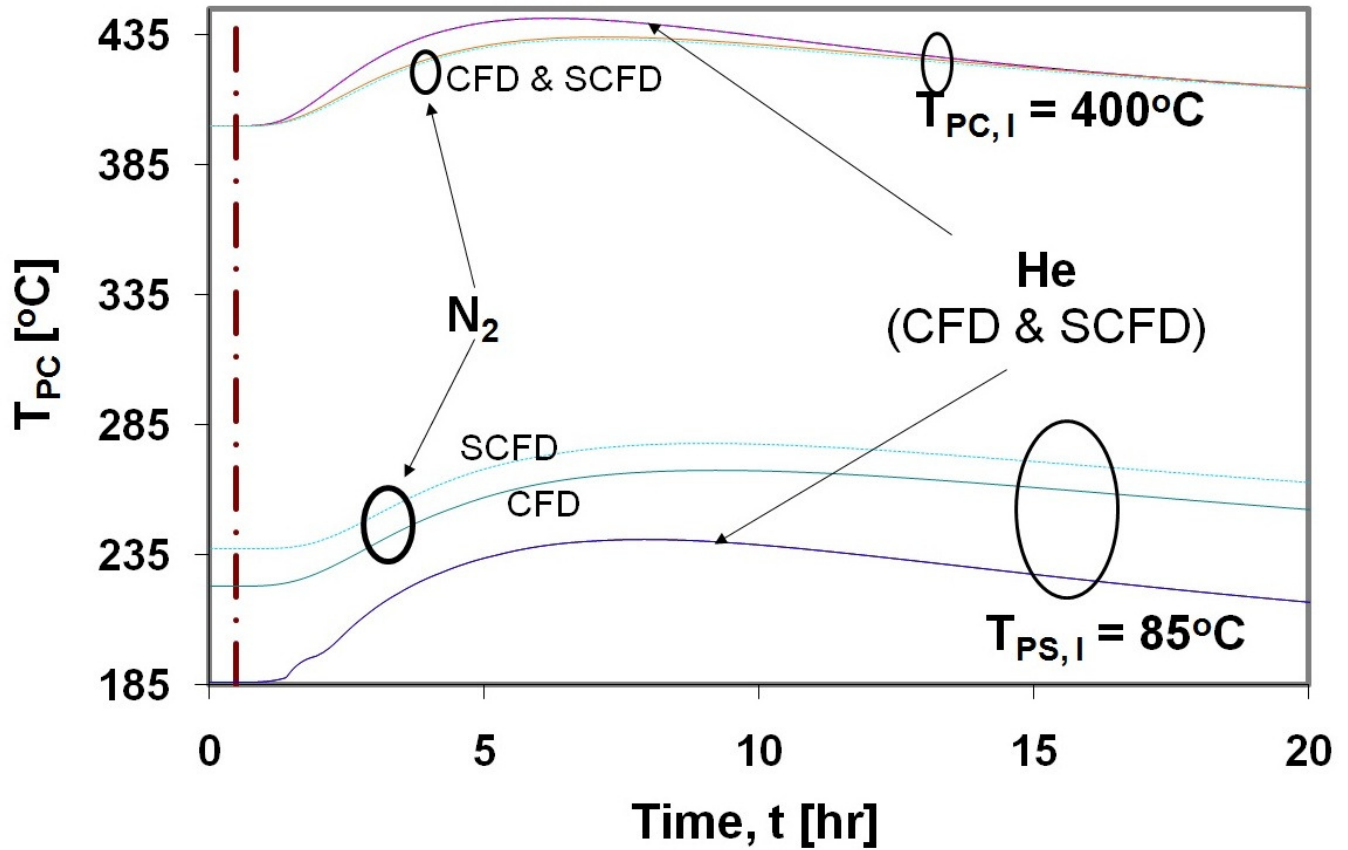


Figure 7: Peak cladding temperature (with Solar Heat Flux) and Peak Surface temperature (without Solar Heat Flux) versus time for different fuel models and cover gases for Regulatory 30 minute fire duration.

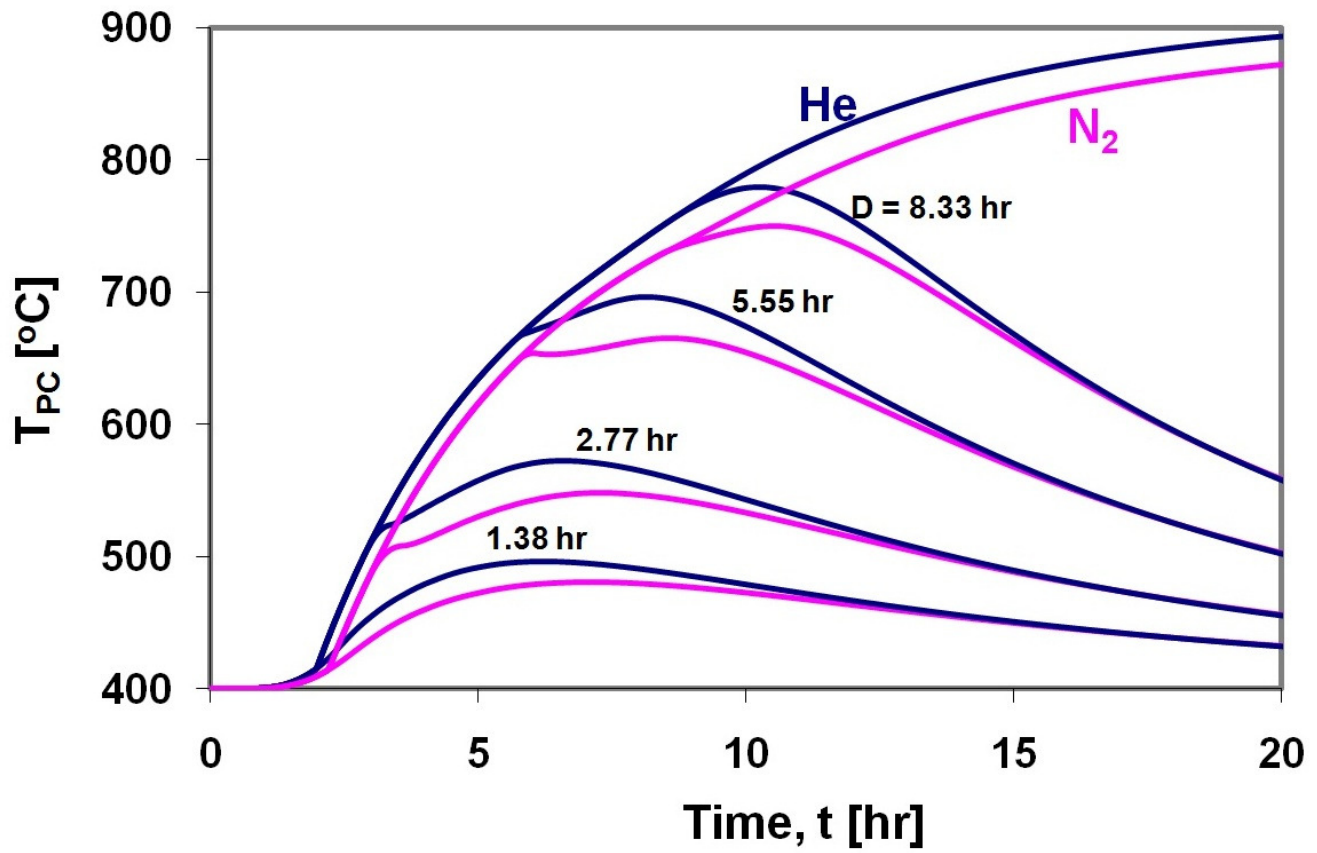


Figure 8: Peak cladding temperature versus duration for different fuel models (CFD and SCFD) and cover gases (Helium and Nitrogen) for different fire durations at initial peak clad temperature, $T_{PC,I} = 400^{\circ}\text{C}$.

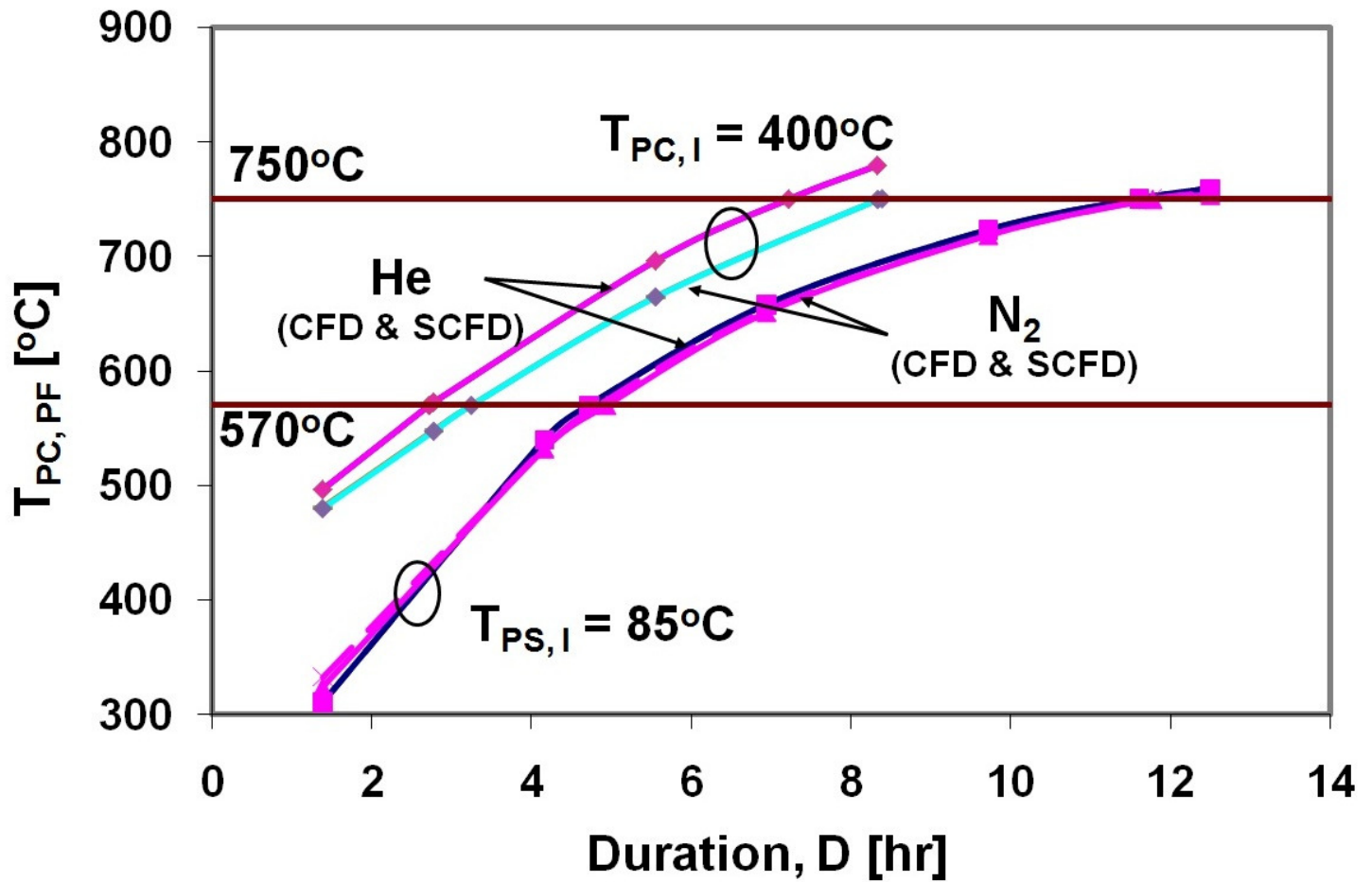


Figure 9: Durations of concern for different fuel models (CFD and SCFD) and cover gases (Helium and Nitrogen).

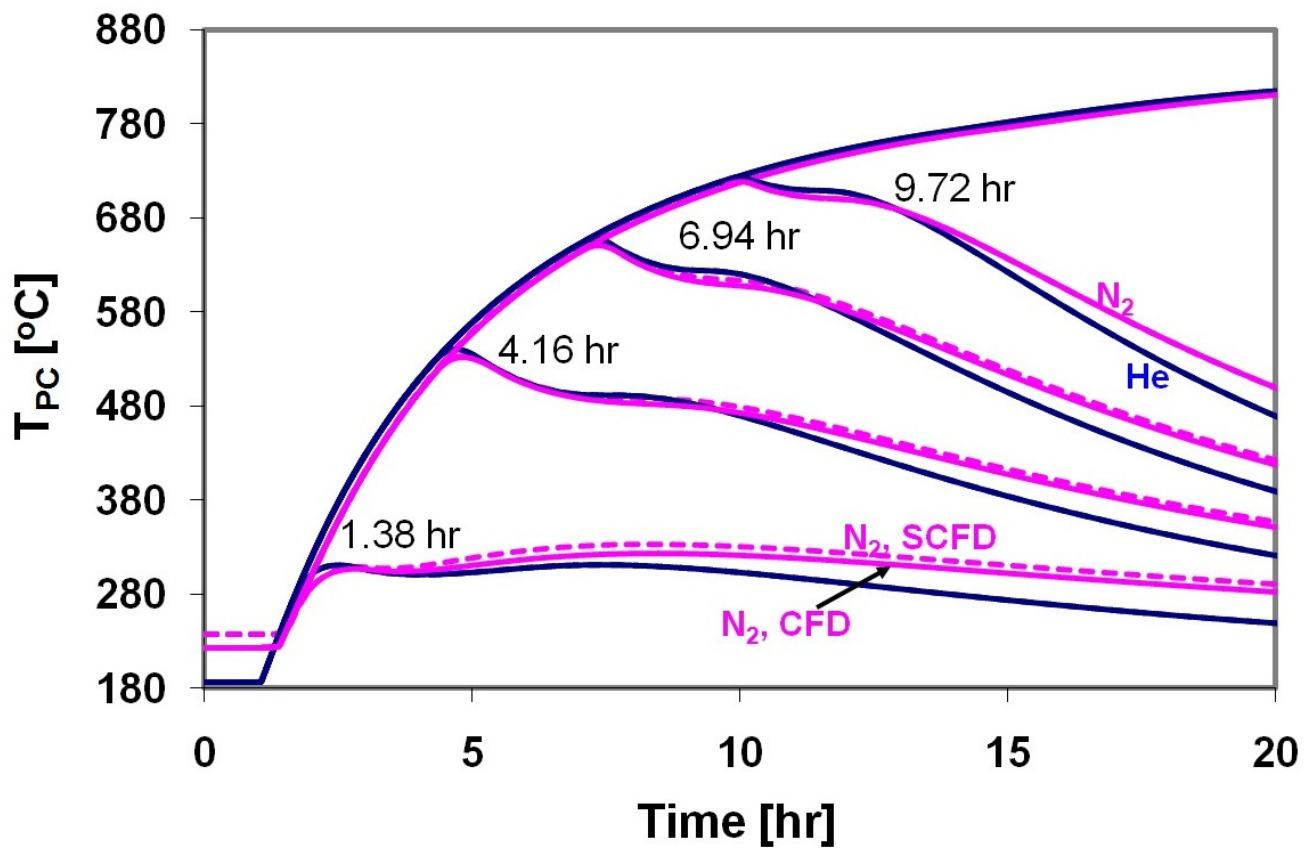


Figure 10: Peak cladding temperature versus duration for different fuel models (CFD and SCFD) and cover gases (Helium and Nitrogen) for different fire durations at initial peak surface temperature, $T_{PS,I} = 85^{\circ}\text{C}$

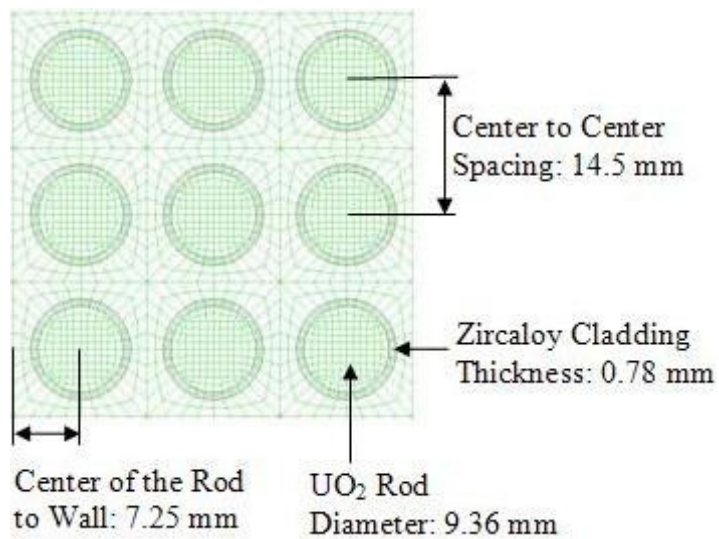
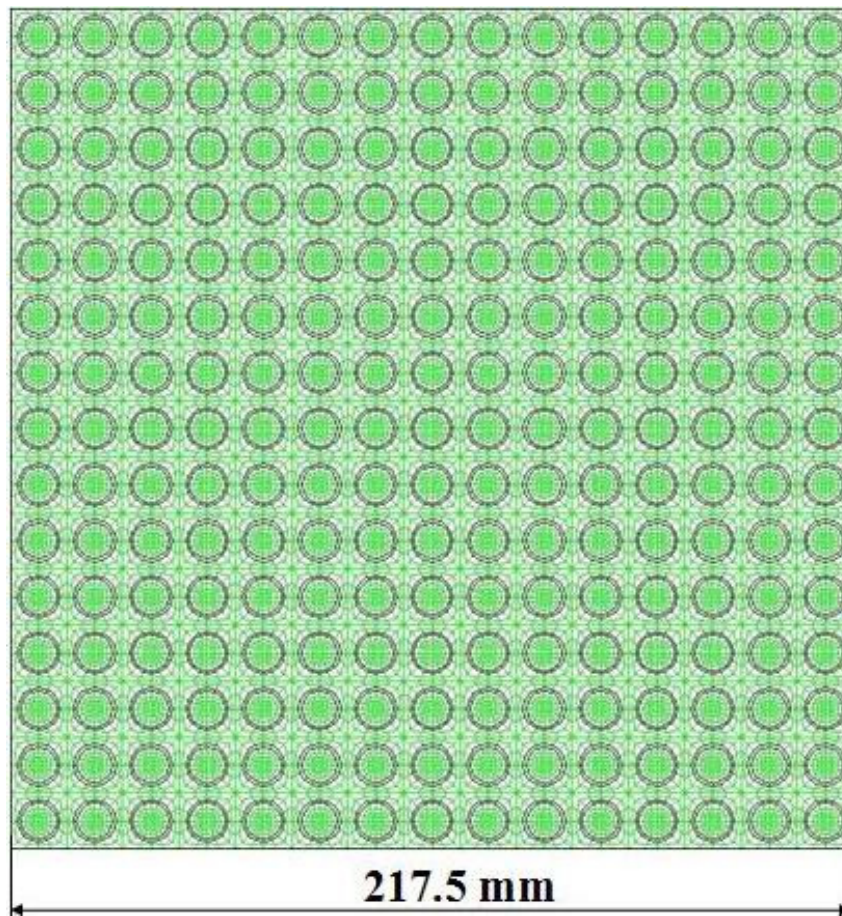


Figure 11: (a) Geometrically-Accurate Isolated Single Fuel Compartment Model, (b) Detail of Coarse Grid with dimensions

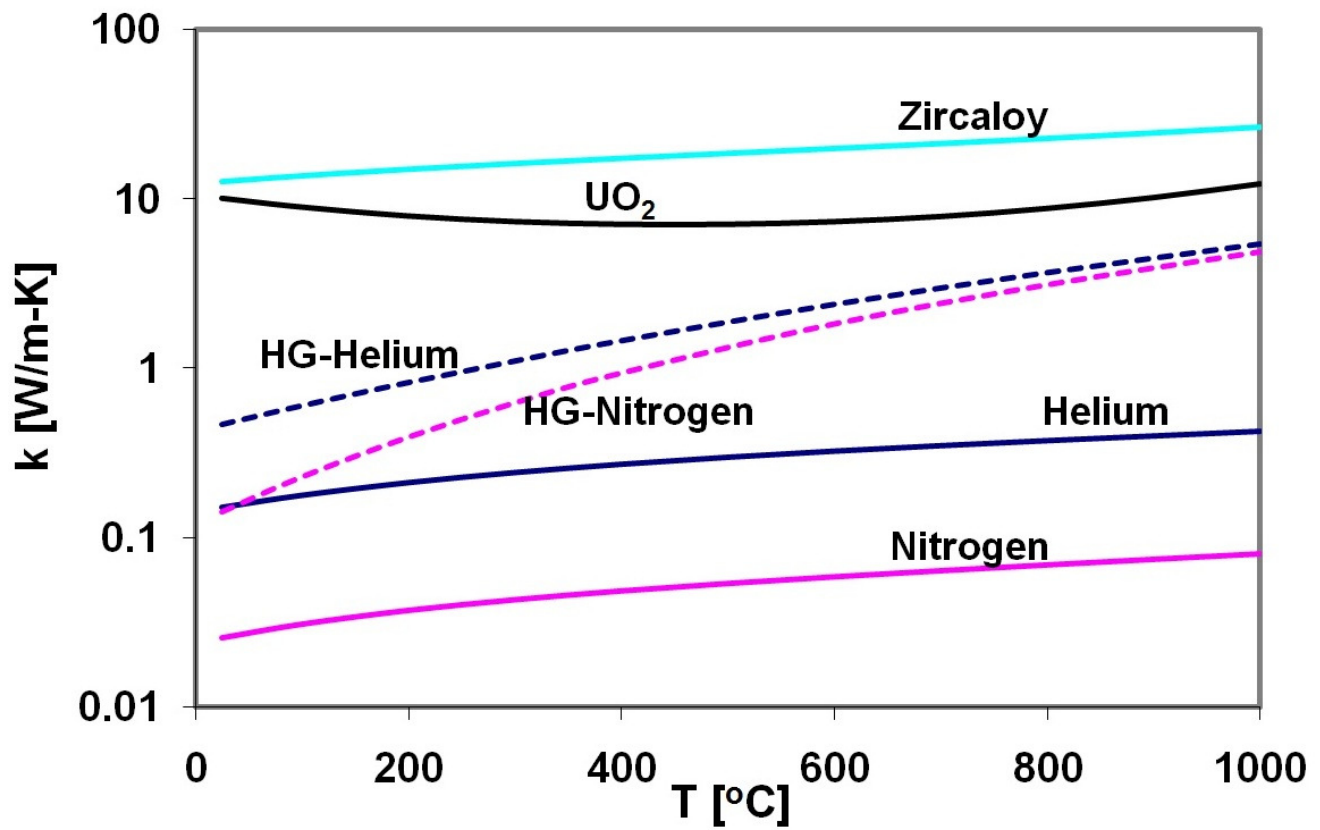


Figure 12: Temperature dependent thermal conductivities for different materials used in 15x15 PWR Isolated fuel compartment model.

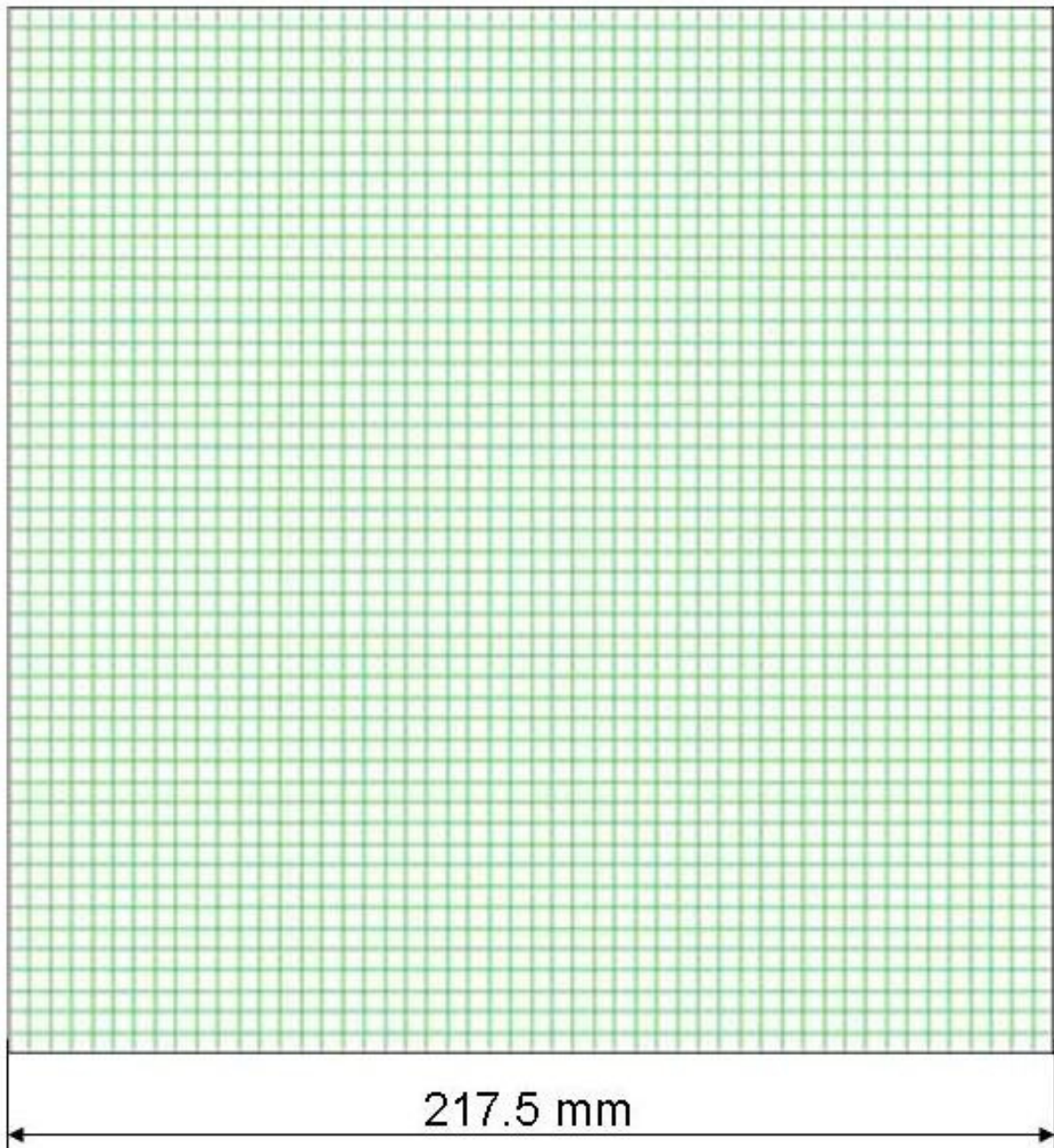


Figure 13: Effective thermal conductivity isolated fuel compartment model

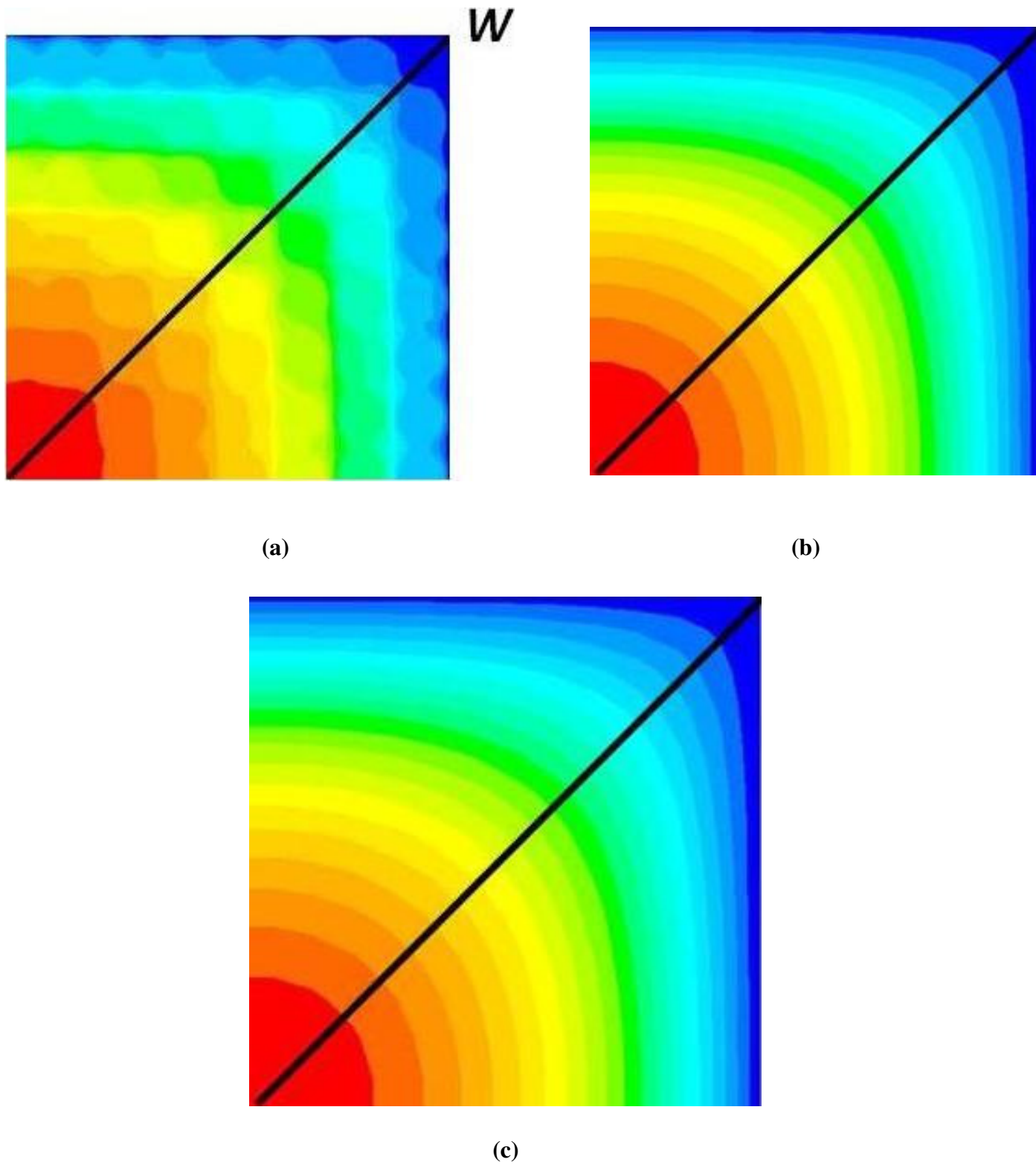


Figure 14: Temperature Contours of a Quarter Geometry for Nitrogen at $T_{\text{WALL}} = 25^{\circ}\text{C}$ and $Q = 432.2 \text{ W}$, (a) AG, (b) HG ($k_U(T_{\text{WALL}}, Q)$) and (c) HG ($K_H(T)$).

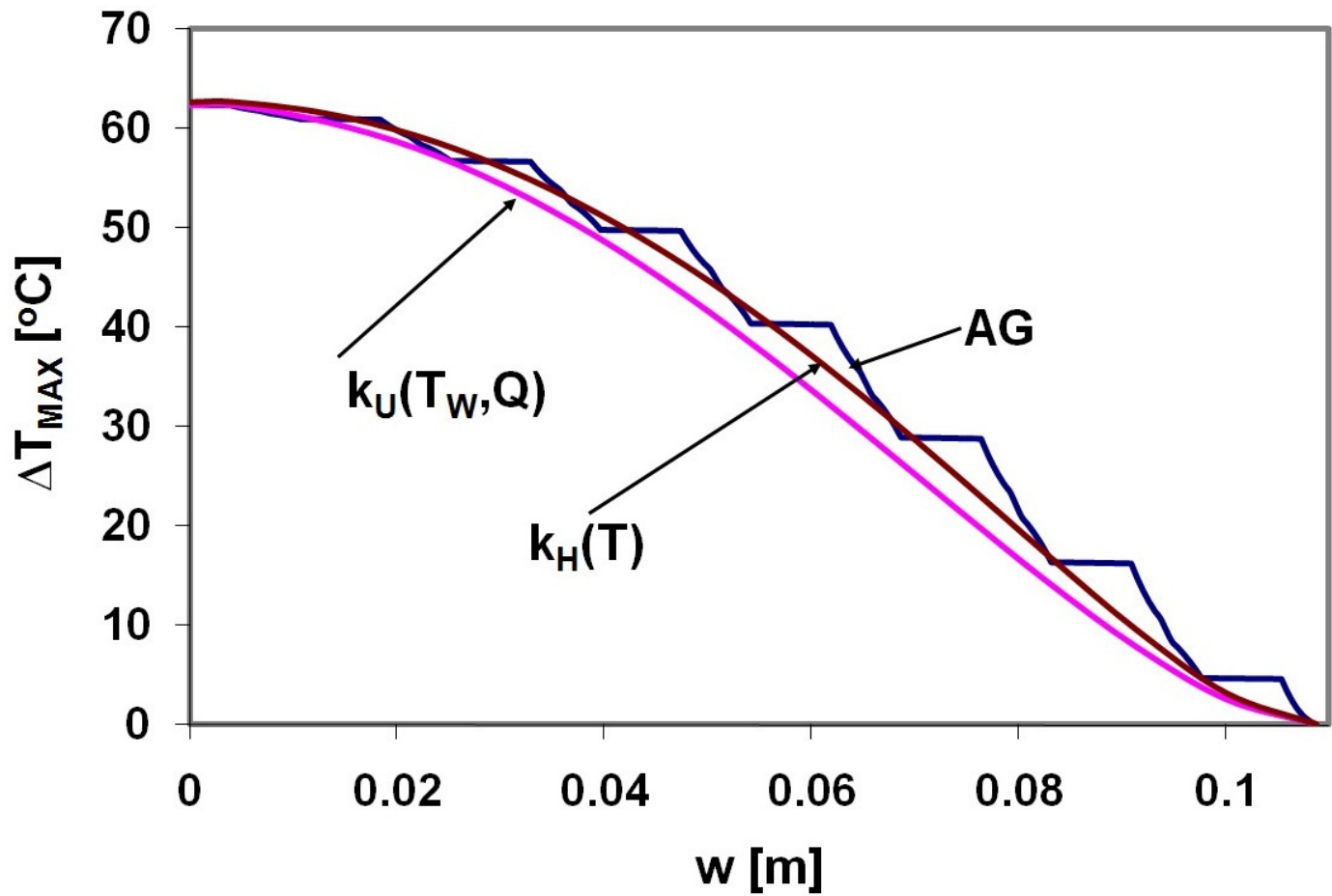
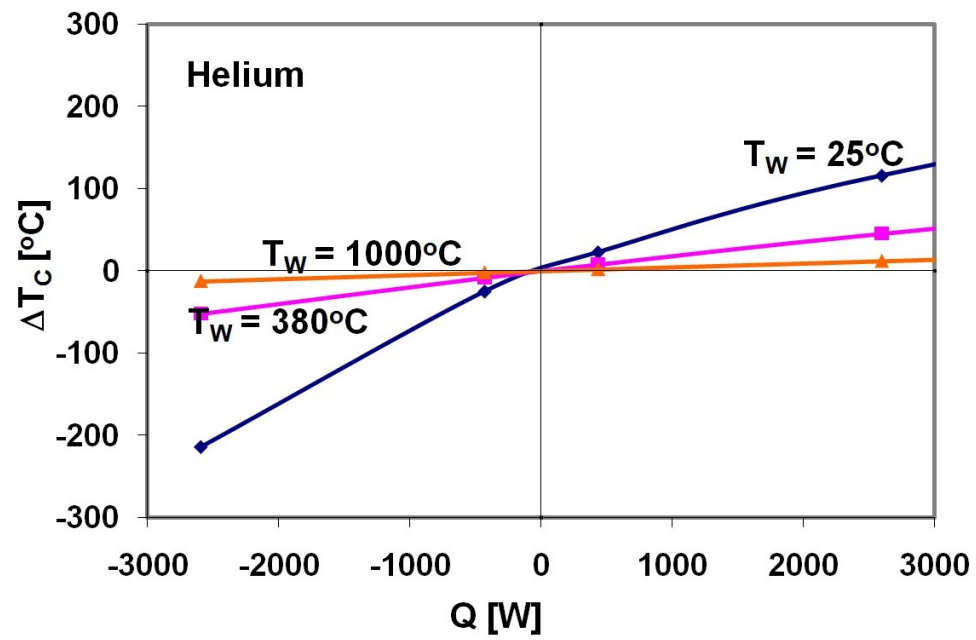
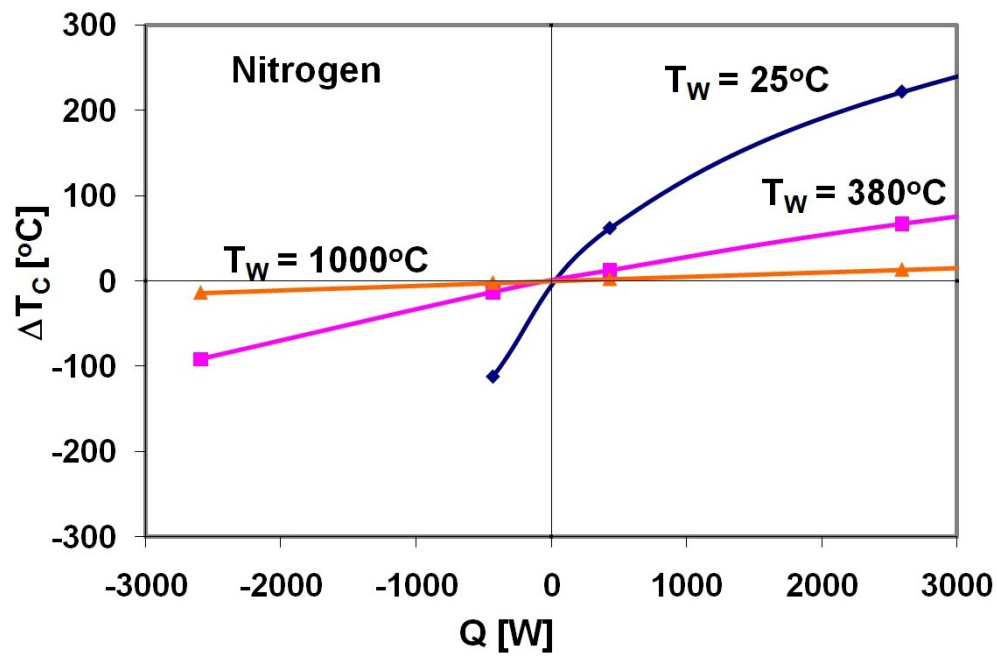


Figure 15: Difference between Maximum temperature and Wall Temperature versus distance from center along the diagonal line shown in Figure 13 for Nitrogen at $T_{WALL} = 25^\circ\text{C}$ and $Q = 432.2\text{ W}$

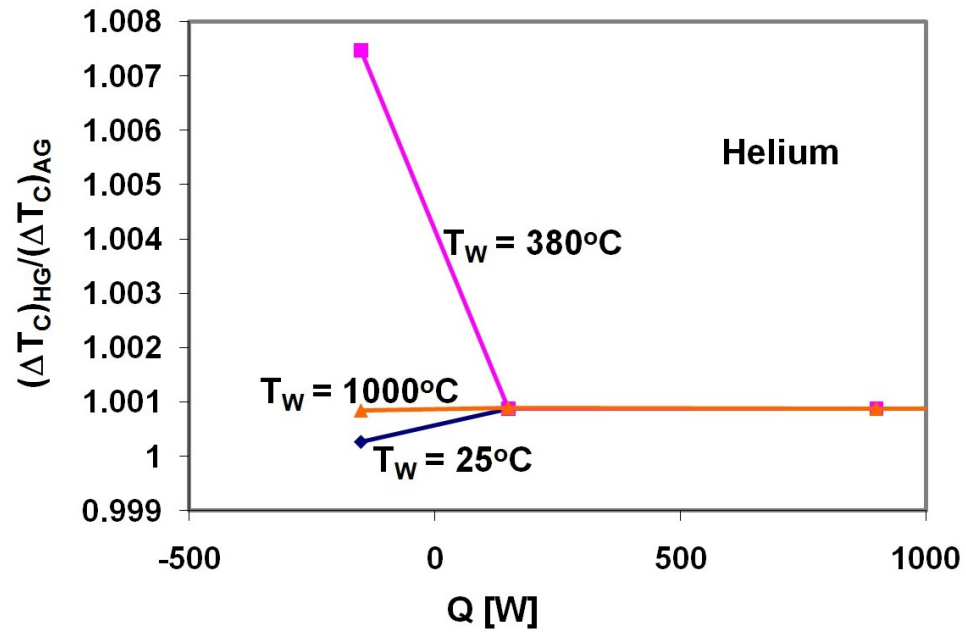


(a)

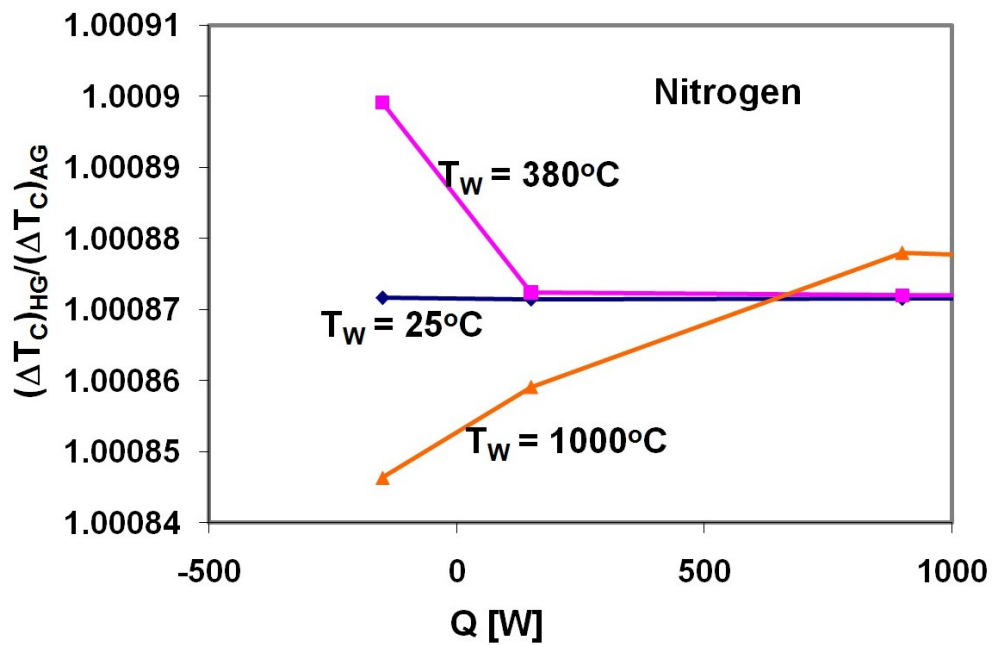


(b)

Figure 16: Difference between Center temperature and Wall Temperature versus heat load at different wall temperatures for (a) Helium and (b) Nitrogen.

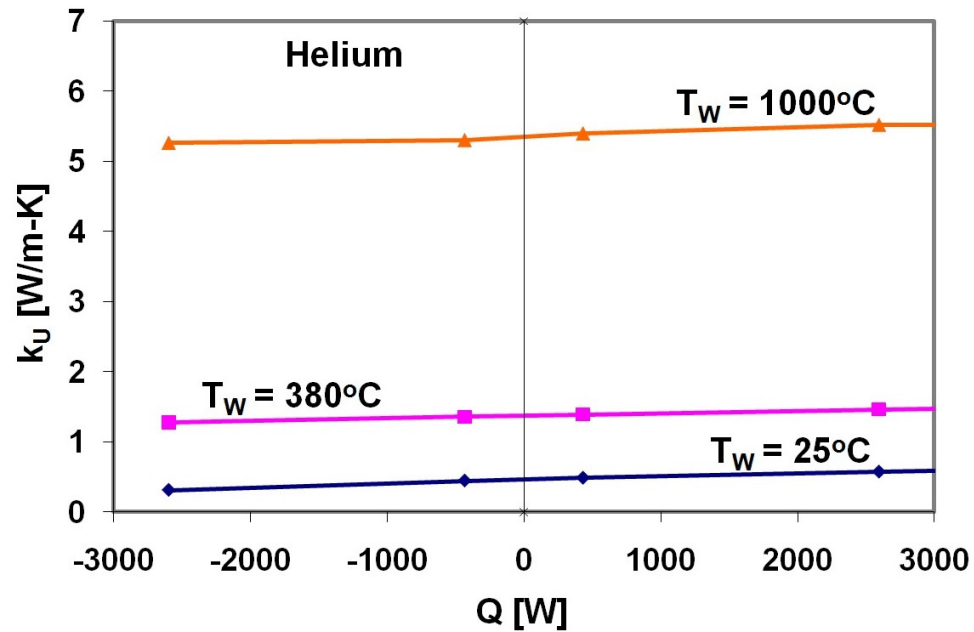


(a)

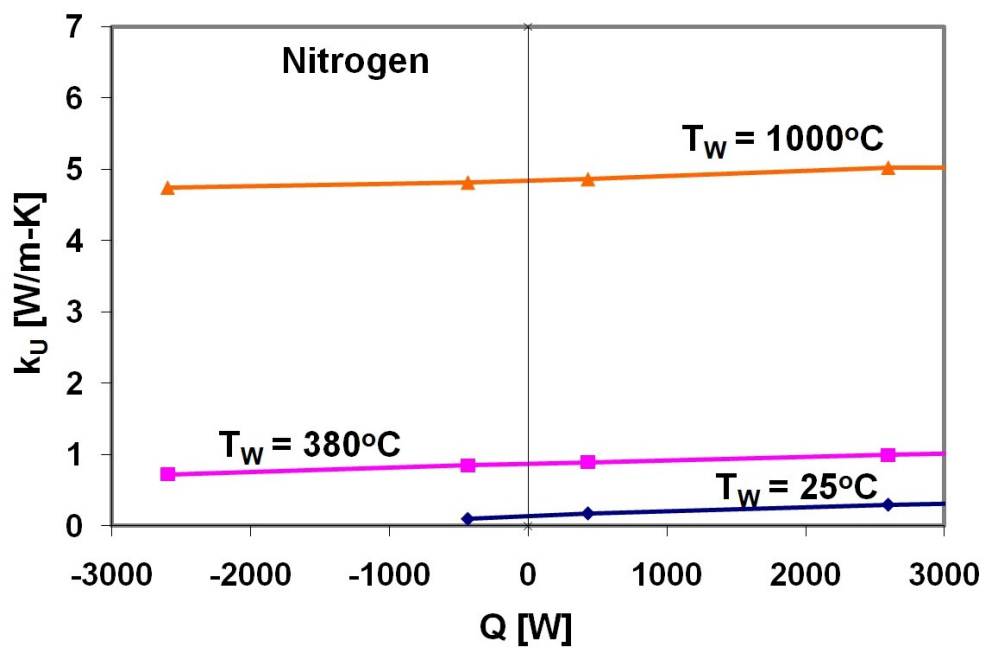


(b)

Figure 17: Ratio of $T_{\text{CENTER}} - T_{\text{WALL}}$ versus heat generation rate for Homogenized geometry and Accurate Geometry for (a) Helium, and (b) Nitrogen



(a)



(b)

Figure 18: Dependence of Global Effective Thermal Conductivity on heat load for different wall temperatures with Angle Discretization value of 8 for (a) Helium and (b) Nitrogen.

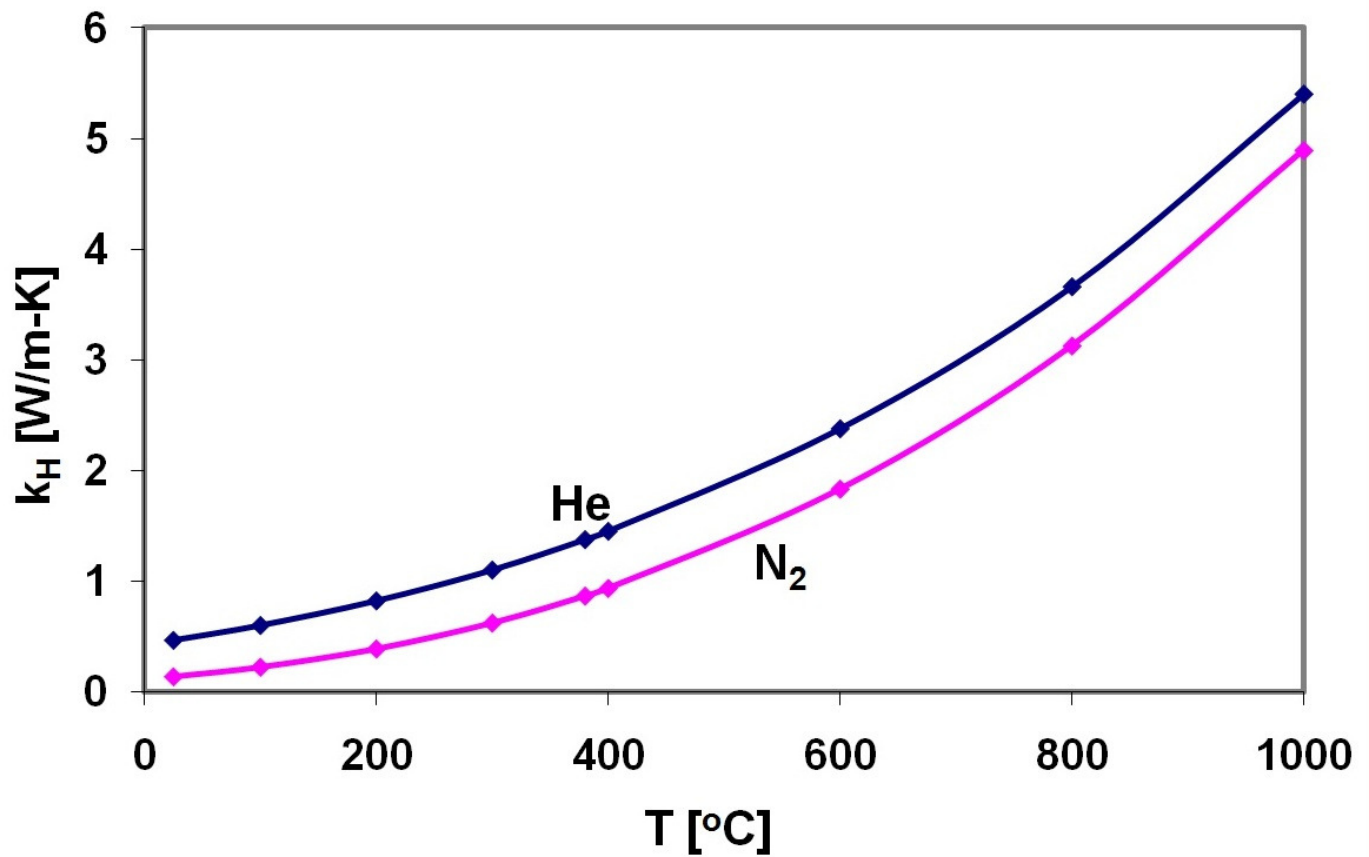


Figure 19: Effective Thermal Conductivity values versus T_{WALL} for Helium and Nitrogen at $Q = 0$ from Figure 18

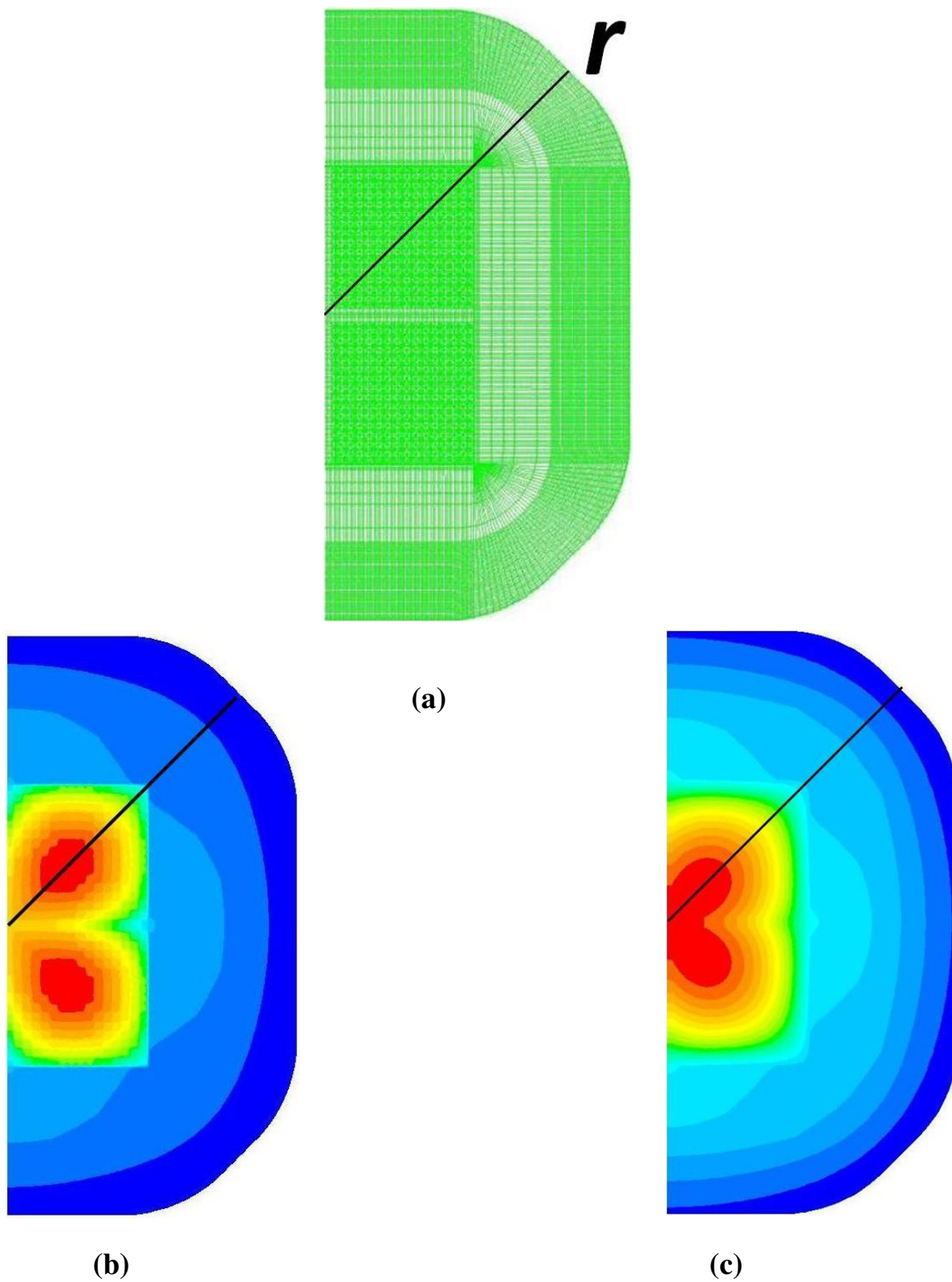


Figure 20: (a) Cross Section of Effective Thermal Conductivity Truck Package, (b) Temperature Contour for AG and (c) Temperature Contour for HG.

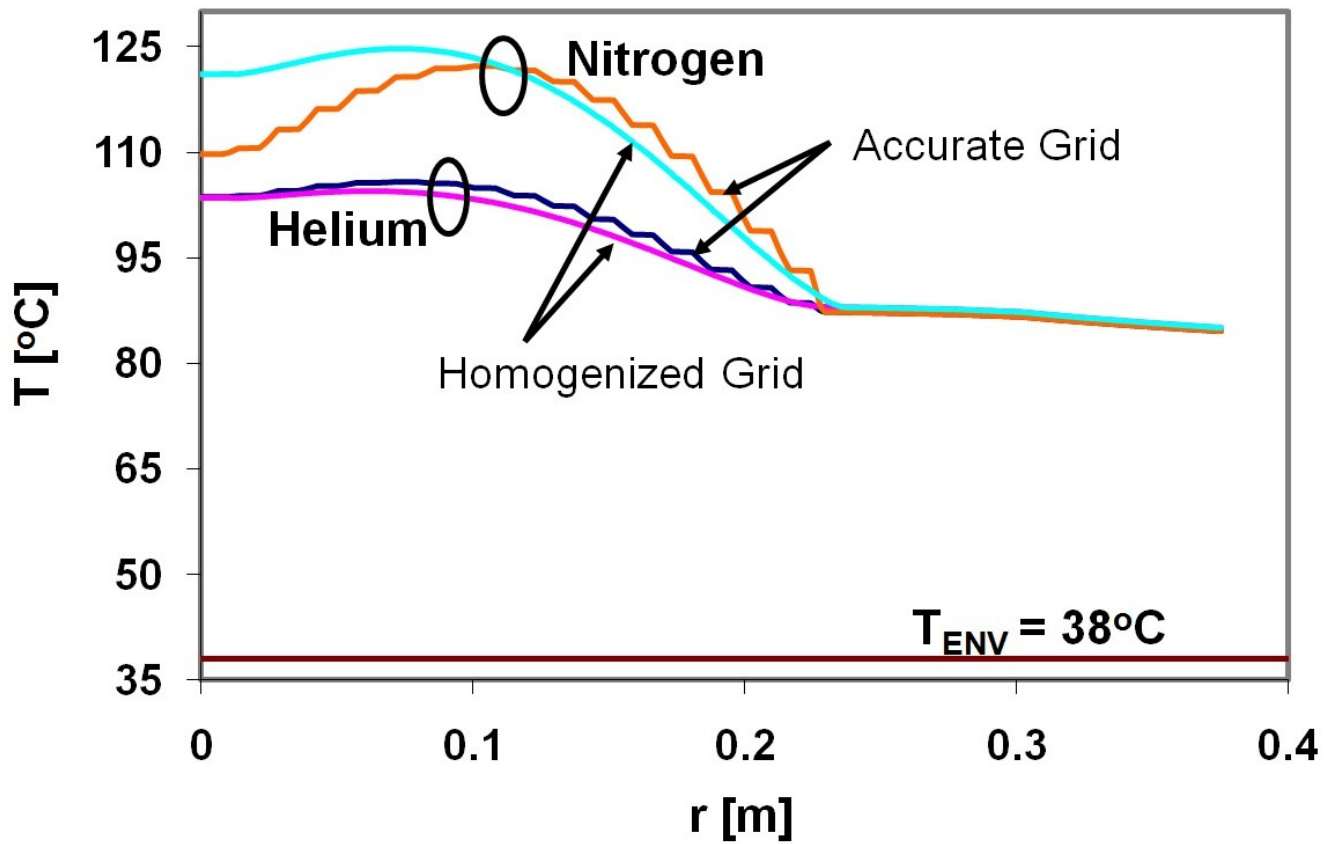


Figure 21: Normal hot day temperature versus distance from the center along the diagonal line shown in Figure 2 for Accurate Grid and Homogenized Grid Models. Environmental temperature, $T_{ENV} = 38^{\circ}\text{C}$ is also shown

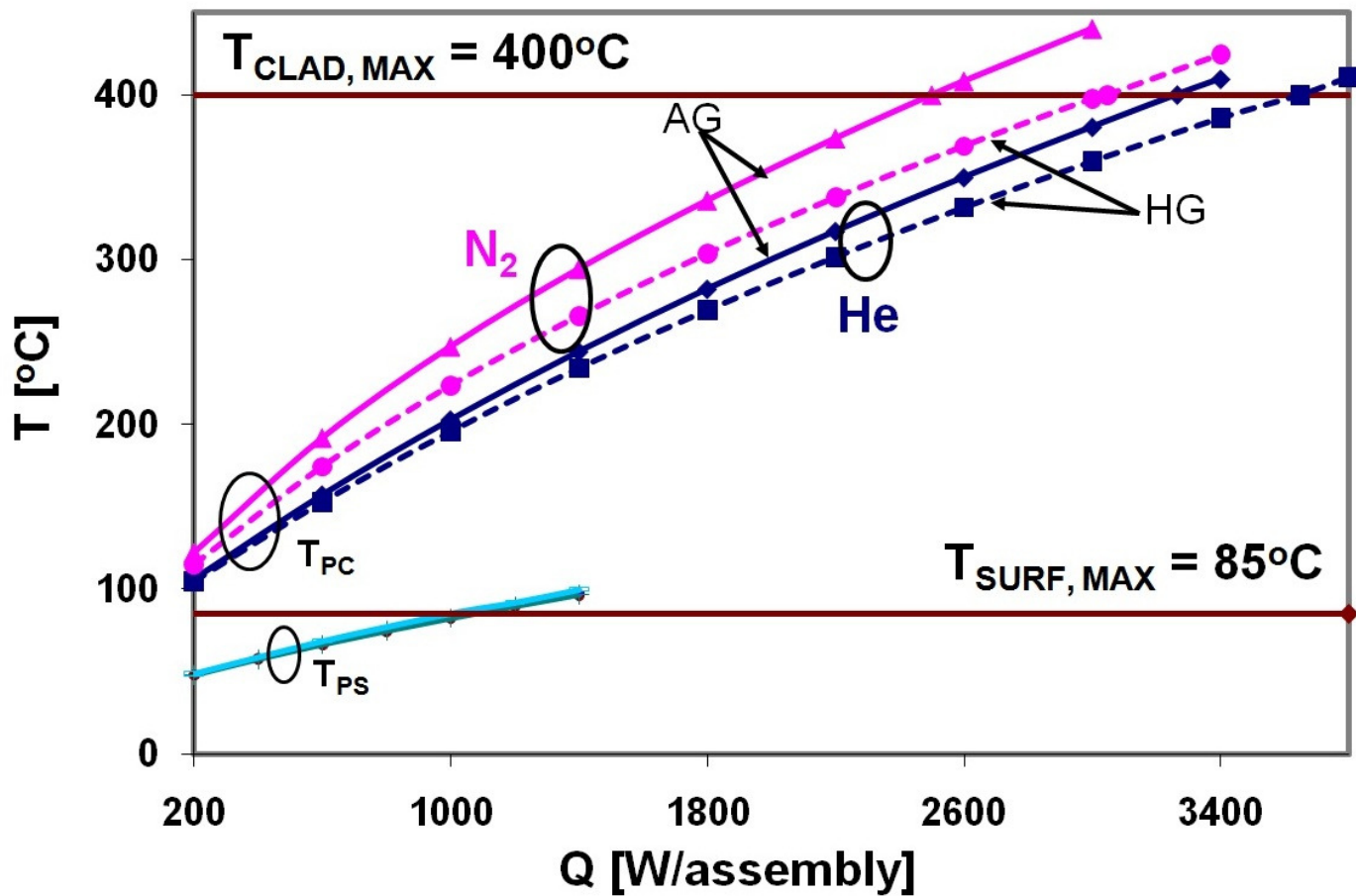


Figure 22: Peak clad temperature (with solar heat flux) and Peak surface temperature (without solar heat flux) versus heat load for LWT cask for different models (Accurate Geometry and Homogenized Geometry) and cover gases (Helium and Nitrogen).

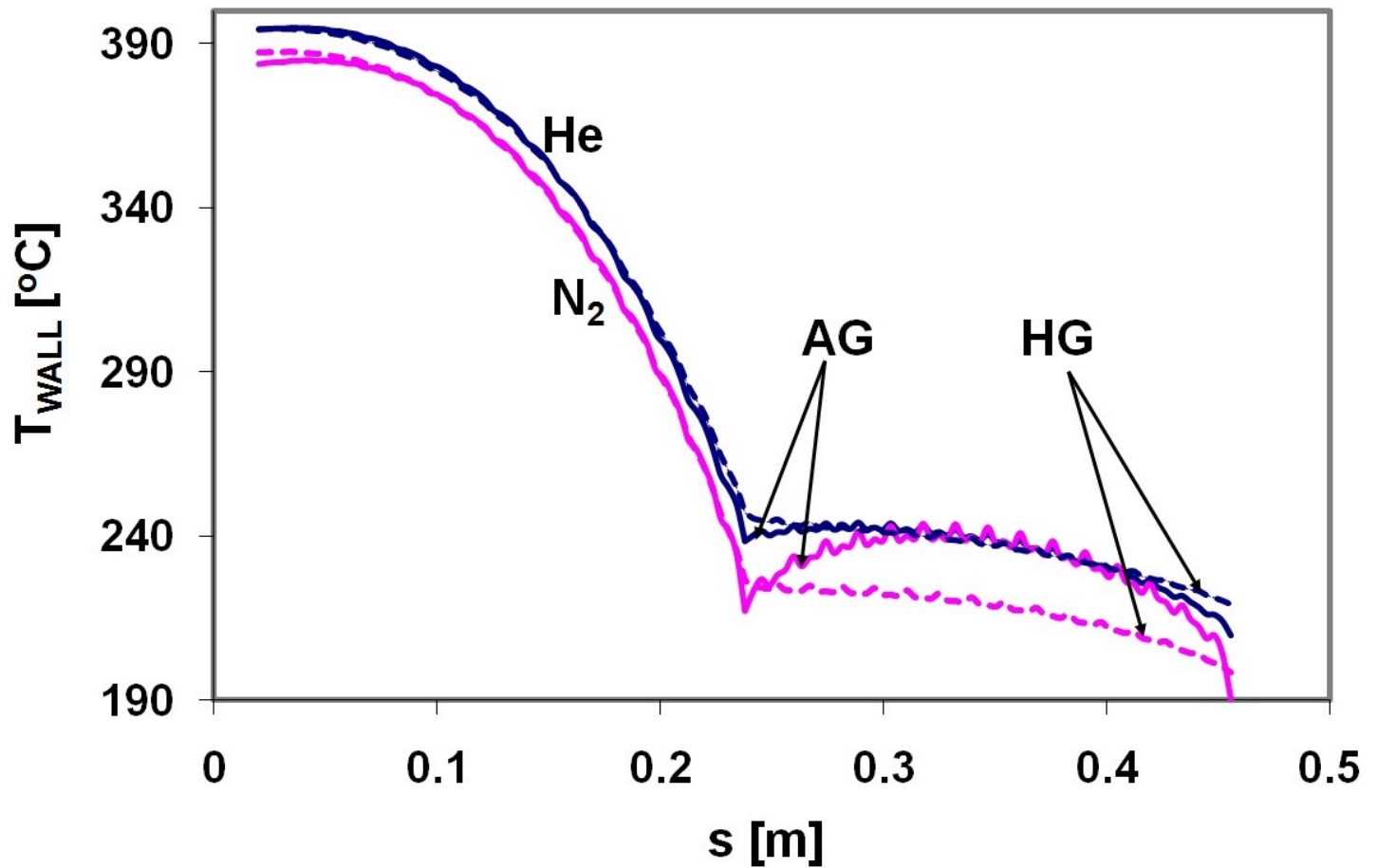


Figure 23: Temperature profiles along the walls of the basket openings versus cord coordinate for N₂ at $Q = Q_{C,N_2}$ and He at $Q = Q_{C,He}$ for Accurate Grid and Homogenized Grid Models

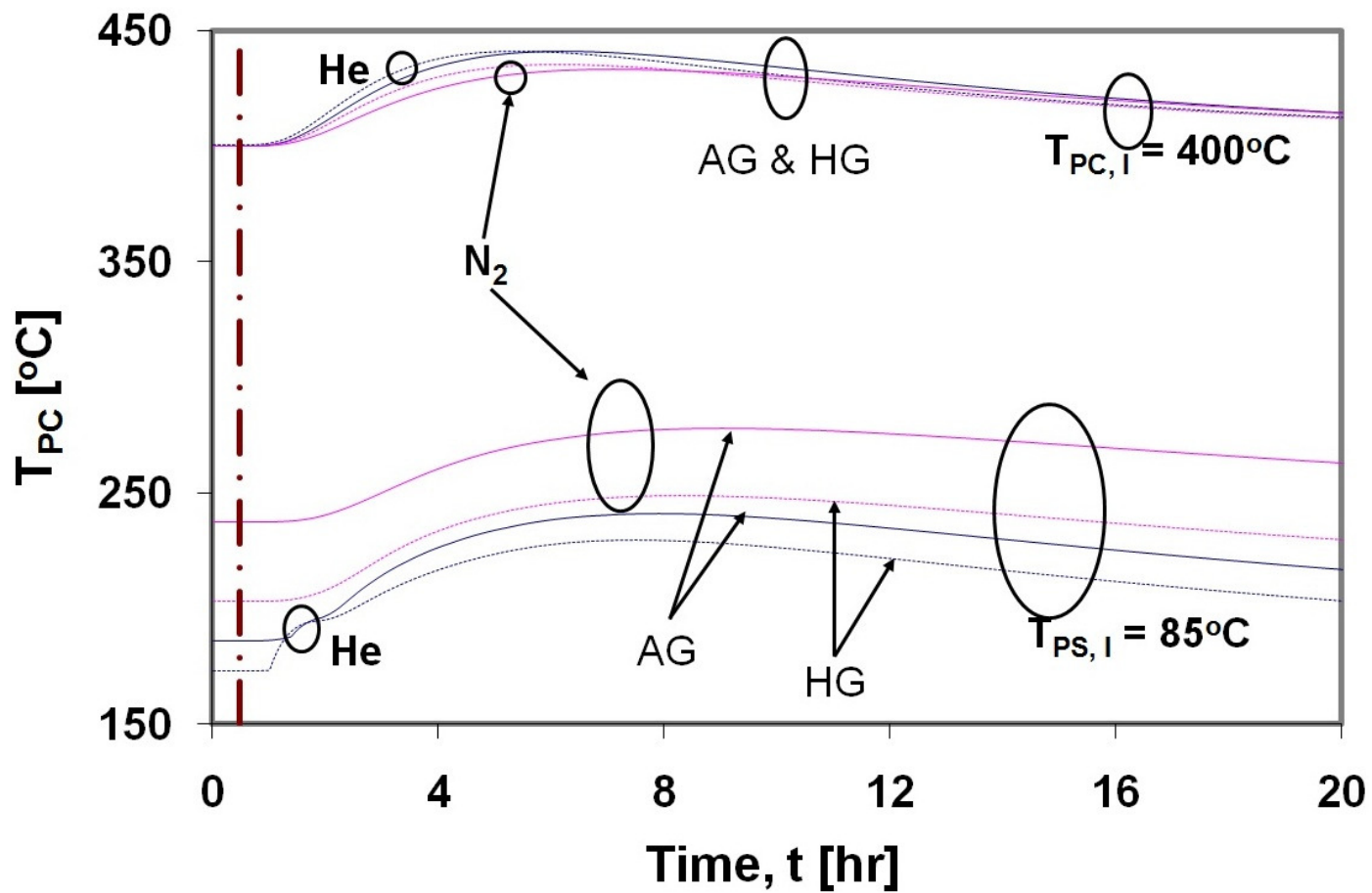


Figure 24: Peak cladding temperature (with and without solar heat flux) versus time for different fuel models (Accurate Geometry and Homogenized Geometry) and cover gases for regulatory 30 minute fire duration.

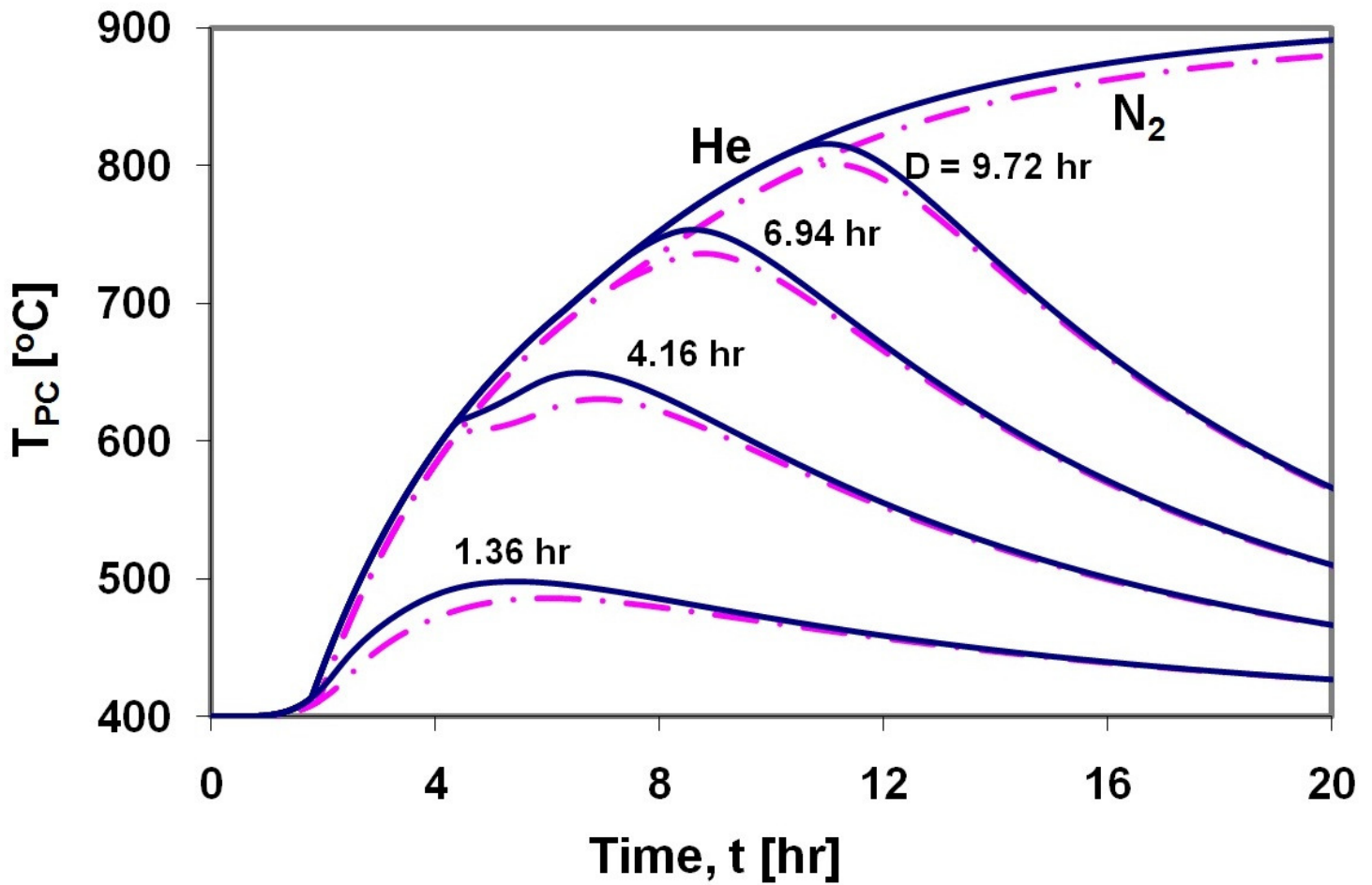


Figure 25: Peak cladding temperature versus time duration for different cover gases (Helium & Nitrogen) and different fire durations at initial peak clad temperature, $T_{PC,I} = 400^{\circ}\text{C}$ for effective thermal conductivity truck cask model.

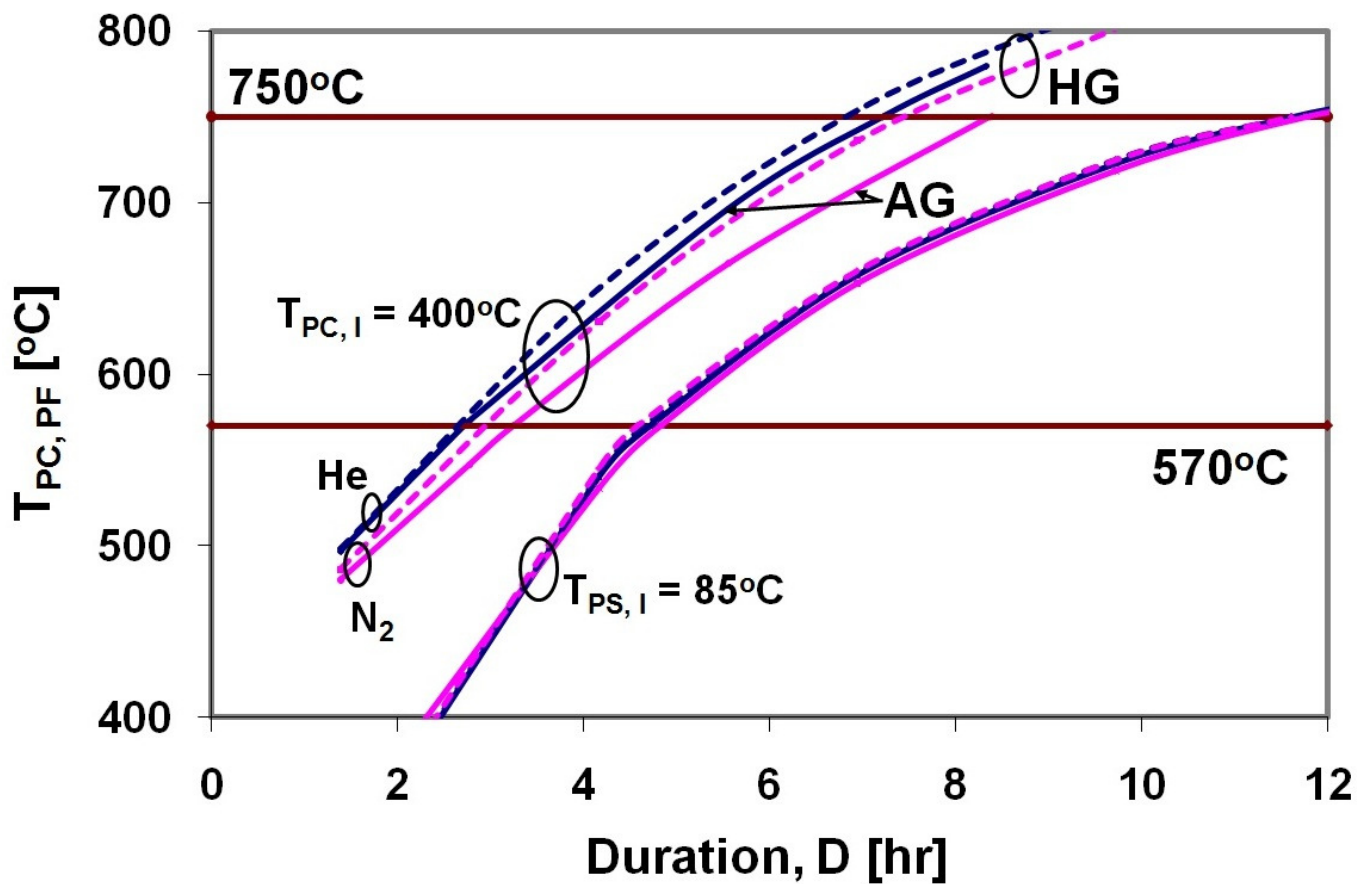


Figure 26: Durations of concern for different fuel models (Accurate Geometry & Homogenized Geometry) and cover gases (Helium & Nitrogen) for two different initial conditions ($T_{PC,I} = 400^\circ\text{C}$ & $T_{PS,I} = 85^\circ\text{C}$).

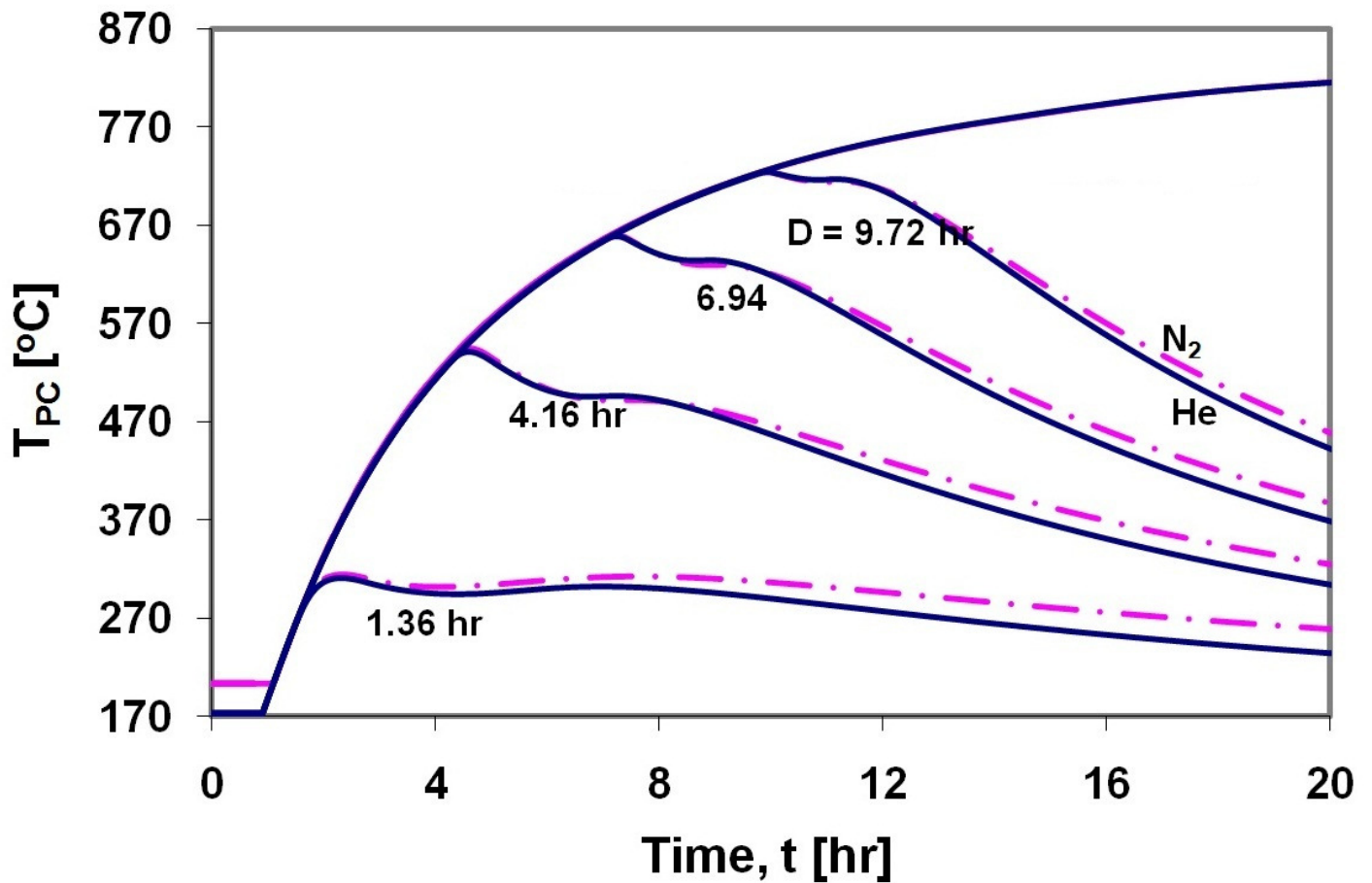


Figure 27: Peak cladding temperature versus time duration for different cover gases (Helium & Nitrogen) and different fire durations at initial peak surface temperature, $T_{PS,I} = 85^{\circ}\text{C}$ for Effective thermal conductivity truck cask model